Secondary reactions of aromatics-derived oxygenated organic molecules lead to plentiful highly oxygenated organic molecules within an intraday OH exposure

Yuwei Wang[1], Chuang Li[1], Ying Zhang[1], Yueyang Li[1], Gan Yang[1], Xueyan Yang[1], Yizhen Wu[1], Lei Yao[1,2], Hefeng, Zhang[3*], Lin Wang[1,2,4,5,6] *

[1] Shanghai Key Laboratory of Atmospheric Particle Pollution and Prevention (LAP[3]), Department of Environmental Science and Engineering, Jiangwan Campus, Fudan University, Shanghai 200438, China

[2] Shanghai Institute of Pollution Control and Ecological Security, Shanghai 200092, China

[3] State Environmental Protection Key Laboratory of Vehicle Emission Control and Simulation, Vehicle Emission Control Center of Ministry of Ecology and Environment, Chinese Research Academy of Environmental Sciences, Beijing 100012, China

[4] IRDR International Center of Excellence on Risk Interconnectivity and Governance on Weather/Climate Extremes Impact and Public Health, Fudan University

[5] National Observations and Research Station for Wetland Ecosystems of the Yangtze Estuary, Shanghai, China

[6] Collaborative Innovation Center of Climate Change, Nanjing, 210023, China

Corresponding Author: H.Z., email, zhanghf@craes.org.cn; phone, +86-10-84915586
L.W., email, lin_wang@fudan.edu.cn; phone, +86-21-31243568

ABSTRACT. Highly oxygenated organic molecules (HOMs) can participate in new particle formation (NPF) and enhance growth of newly formed particles partially because of their low volatility. Previous studies have shown formation of HOMs via autoxidation reactions of RO_2 intermediates generated by OH-initiated oxidation of anthropogenic volatile organic compounds (VOCs). It was also suggested that multi-generation OH oxidation could be an important source for aromatics-derived HOMs. However, our understanding on the generation of aromatics-derived HOMs are still insufficient, especially for their formation mechanisms, which determine molar yields of HOMs and are essential to the establishment of global chemical box models related to HOMs. In this study, with a potential aerosol mass oxidation flow reactor (PAM OFR), two series of OH-initiated oxidation experiments of 1,3,5-trimethylbenzene (1,3,5-TMB) were conducted to investigate the formation of aromatics-derived HOMs. In the first series, the evolution of oxidation products of 1,3,5-TMB in an OH exposure range of $(0.5 – 5.0)\times10^{10}$ molecules cm^{-3} s, equivalent to an OH exposure of $0.7 – 6.9$ hours at an OH concentration ([OH]) of 2×10^6 molecules cm^{-3}, was investigated by a nitrate-based chemical ionization mass spectrometer and a Vocus proton-transfer-reaction mass spectrometer, indicating significant secondary OH chemistry during the ageing of stabilized

1

first generation oxygenated products within an intraday OH exposure and formation of various HOMs with lower double bond equivalence (DBE). In addition, organonitrates, formed after the introduction of NO_x into the reaction systems, further confirmed the existence of such secondary reactions. The second series of experiments was conducted with same residence time but much lower [OH], which also shows the generation of multi-generation HOMs with an [OH] as low as 1.06×10^7 molecules cm^{-3} for 53 s, i.e., an OH exposure of around 5.86×10^8 molecules cm^{-3} s. Our study suggests an important role of secondary OH chemistry in the oxidation of aromatics, if these oxygenated products survived long enough in the ambient, and elucidates detailed formation mechanisms of certain HOM products.

1 Introduction

OH radicals can react with volatile organic compounds (VOCs) in the atmosphere, converting primary pollutants to secondary ones. Generated from oxidation of VOCs, oxygenated organic molecules (OOMs) are crucial in a variety of atmospheric chemical processes, contributing efficiently to the formation of secondary organic aerosols (SOAs) and ground-level O_3 (Ng et al., 2010; Wang et al., 2022; Qu et al., 2021). Among the enormous number of oxygenated VOCs (OVOCs), highly oxygenated organic molecules (HOMs) have recently attracted significant attention (Bianchi et al., 2019). Most of HOMs are low volatility organic compounds (LVOCs) or extremely low volatility organic compounds (ELVOCs), and thus are able to drive the initial formation of nucleated particles under certain conditions and contribute to the subsequent growth of newly-formed particles, which finally enhance SOA formation (Tröstl et al., 2016; Lehtipalo et al., 2018; Stolzenburg et al., 2018; Mohr et al., 2019; Qiao et al., 2021).

Formation of HOMs is triggered by oxidation of VOCs in the gas phase. Peroxy radicals (RO_2) are generated at the initial step and will undergo an intramolecular hydrogen atom shift forming a hydroperoxide functionality and an alkyl radical. A molecular oxygen will rapidly attach to this alkyl radical and form a new and more oxidized RO_2. This reaction is called as autoxidation and the newly formed RO_2 can go through another autoxidation or bimolecular termination reactions to form a stabilized product (Crounse et al., 2013). Autoxidation is suggested to be responsible for widely detected HOMs in the atmosphere, because it can form highly oxygenated RO_2 in a short time scale. In terms of biomolecular reactions, RO_2 reacts appreciable only with hydroperoxyl radical (HO_2), NO, and another RO_2. The RO_2 reaction chain in polluted areas is largely terminated by NO, which prohibits generation of compounds with high oxidation levels and reduces yields of HOMs (Bianchi et al., 2019).

70   Nevertheless, autoxidation reactions alone are not enough to explain the large numbers of

71   oxygen atoms and low double bond equivalence (DBE, calculated as $nC - \frac{nH+nN}{2} + 1$ where

72   nC, nH, and nN stand for the number of carbon, hydrogen, and nitrogen atoms, respectively, in

73   a molecular) for HOMs observed in laboratory experiments and ambient campaigns. Take

74   alkylbenzenes as an example, previous studies suggest that the main products of OH-initiated

75   oxidation of alkylbenzenes (C_xH_{2x-6}, x=7, 8, or 9), i.e., bicyclic peroxy radicals (BPR, $C_xH_{2x-5}O_5\cdot$, x=7, 8, or 9) (Jenkin et al., 2003), can undergo an autoxidation reaction and form a new

76    $_5O_5\cdot$, x=7, 8, or 9) (Jenkin et al., 2003), can undergo an autoxidation reaction and form a new

77   peroxy radical, $C_xH_{2x-5}O_7\cdot$ (x=7, 8, or 9) (Wang et al., 2017).Autoxidation of BPR could be

78   very fast if it has a favorable structure, as found in a previous study (Wang et al., 2017). On the

79   other hand, the structure of the resulting $C_xH_{2x-5}O_7\cdot$ is strongly different from that of BPR,

80   whose autoxidation reaction rate can be as low as the order of 0.001 s^{-1}, since it lacks

81   enhancements from favorable transition state geometries and substitutes or resonance structures

82   (Bianchi et al., 2019; Otkjær et al., 2018). Such a slow autoxidation reaction rate cannot explain

83   the extensive existence of HOM monomers with more than 7 oxygen atoms and HOM dimers

84   with more than 10 oxygen atoms, which are the maximum numbers of oxygen atoms in

85   stabilized first generation monomer and dimer products, respectively, formed from $C_xH_{2x-5}O_7\cdot$ (Molteni et al., 2018; Wang et al., 2020b; Mentel et al., 2015; Berndt et al., 2018b).

86    $_5O_7\cdot$ (Molteni et al., 2018; Wang et al., 2020b; Mentel et al., 2015; Berndt et al., 2018b).

87   Another possibility is the formation of a second oxygen bridge after the hydrogen shift of BPR

88   (Molteni et al., 2018), but this reaction pathway would not allow a further oxygenation reaction

89   without a breakage of the carbon ring, which is also unpromising. A very recent investigation

90   offers new insights into the formation mechanism of these products, indicating the molecular

91   rearrangement of BPR can initiate a series of autoxidation (Iyer et al., 2023). However, the

92   formation mechanism of HOMs with a large hydrogen atom number, i.e., low DBE, is still

93   vague. For example, monomer products with 16 hydrogen atoms in the OH-initiated oxidation

94   of TMB and those with 14 hydrogen atoms in the OH-initiated oxidation of xylene were

95   observed in the laboratory, both with a DBE of 2 lower than their precursors' (Molteni et al.,

96   2018), but their formation mechanisms cannot be explained by any known mechanisms with

97   only one OH attack.

98   Multigeneration reactions of VOCs complicate HOMs' formation. Previous studies

99   indicate that HOMs can also be formed by sequential oxidation of stabilized first-generation

100   products of benzene and toluene (Garmash et al., 2020; Cheng et al., 2021). Garmash et al.

101   (2020) conducted OH oxidation experiments of benzene and toluene with an OH exposure

102   equivalent to atmospheric oxidation times of 10 hours – 15 days at OH concentrations of ~10^6

103   molecules cm^{-3}. Cheng et al. (2021) simulated oxidation of benzene and toluene with an OH

104   exposure equivalent to 2.4 – 19.4 days of atmospheric photochemical ageing. Certainly, such

105   extremely high OH exposures favor secondary OH chemistry and help to facilitate our

106   understanding on product distributions, but such a long timescale limits atmospheric

107   implications of their results, given the complex physical and chemical processes that occur at

108   night.

109   Compared to benzene and toluene, trimethylbenzene (TMB) is a compound characterized

110   with much larger HOM molar yields when reacted with OH, and the abundance of TMB in the

111   atmosphere is unignorable (Molteni et al., 2018; Yuan et al., 2012). Previous laboratory

112   experiments on TMB-derived HOMs mainly focused on the autoxidation reactions of BPR and

113   the influences of NO_x, and the quantity of experiments was very finite, restricting the

114   application of their conclusions to atmospheric relevant conditions (Tsiligiannis et al., 2019;

115   Wang et al., 2020b). From the mechanism perspective, a number of HOM monomers with more

116   than 7 oxygen atoms detected in the OH-initiated oxidation of TMB were previously assumed

117   to be generated via multiple autoxidation reactions (Molteni et al., 2018). Nevertheless, a

118   subsequent OH oxidation of the first-generation oxygenated products might be more plausible

119   for the formation of HOM monomers with more than 7 oxygen atoms from the present point of

120   view. Indeed, laboratory experiments show that RO_2 formed during the second-generation OH

121   oxidation of the stabilized first-generation oxidation products can also undergo autoxidation

122   reactions, which entangles reaction mechanisms potentially involved in the formation of those

123   HOMs and justifies more investigations on the multigeneration OH oxidation of aromatics

124   (Wang et al., 2020b). Atmospheric OH concentration ([OH]) up to $6\times10^6 - 2.6\times10^7$ molecule

125   cm^{-3}, which is several times higher than the typical average atmospheric [OH], 1.5×10^6

126   molecule cm^{-3} (Jacob, 1999), has been frequently observed in both urban and suburban

127   environments in China (Tan et al., 2019; Lu et al., 2012), leading to a realistic implication of

128   multigeneration OH oxidation. Therefore, it is imperative to study chemical characteristics of

129   aromatics-derived HOMs at different OH exposures, especially those that are less than or

130   equivalent to one day of atmospheric oxidation.

131   In this study, two series of laboratory experiments on OH-initiated oxidation of 1,3,5-TMB,

132   selected as an example of anthropogenic VOCs, were conducted. One was conducted with [OH]

133   ranging from 9.32×10^7 to 1.03×10^9 molecule cm^{-3}, corresponding to an OH exposure equivalent

134   to atmospheric oxidation times of roughly 0.7 – 6.9 hours at an average daytime [OH] of $2.0\times$

135   10^6 molecules cm^{-3}. A nitrate-based chemical ionization mass spectrometer (nitrate CIMS) and

136   a Vocus proton-transfer-reaction mass spectrometer (Vocus PTR) were deployed to measure

137   the oxidation products and the precursor, respectively. We explored the evolution of oxidation

138   products to investigate the secondary OH chemistry of stabilized first-generation oxidation

139   products generated by the oxidation of 1,3,5-TMB. Furthermore, the influence of NO on the

140   formation of HOMs was investigated by introducing N_2O into the reaction system. In addition,

141   another series of experiments under atmospheric relevant [OH] were conducted to confirm the

142   applicability of the above-developed multi-generation OH oxidation mechanisms in the

143   ambient atmosphere.

144   **2 Methods**

145   OH-initiated oxidation of 1,3,5-TMB was investigated in a potential aerosol mass

146   oxidation flow reactor (PAM OFR) system at $T = 298 \pm 1$ K and a pressure of 1 atm (Lambe et

147   al., 2015). Two series of experiments were conducted, one under high [OH] conditions and the

148   other under low [OH] conditions. Hereafter, we refer to the series of high [OH] experiments as

149   'the 1st-round experiments' and the low [OH] ones as 'the 2nd-round experiments', respectively.

150   The ith experiment in the 1st-round experiments is labelled as 1-i and the one in the 2nd-round

151   experiments as 2-i, where i stands for its serial number. The experimental settings in this study

152   differed slightly from what were used previously (Wang et al., 2020b). In the 1st-round

153   experiments, forty OH experiments without NO_x (Exp. 1-1 – 1-40) and twenty-eight

154   experiments with NO_x (Exp. 1-41 – 1-68) were performed. Seven experiments were conducted

155   in the 2nd-round, four without NO_x (Exp. 2-1 – 2-4) and three with NO_x (Exp. 2-5 – 2-7). The

156   experimental conditions are summarized in Table S1, including concentrations of the precursor,

157   ozone, and NO and NO_2. The equivalent OH exposure in the OFR for each experiment was

158   estimated according to the precursor consumption, and also listed in Table S1. OH exposures

159   in the OFR were in the range of $(5.2 – 48.7) \times 10^9$ and $(0.6 – 5.5) \times 10^9$ molecules cm^{-3} s in the

160   1st-round and 2nd-round experiments, respectively.

161   A home-made 1,3,5-TMB/N_2 cylinder was used as a stable gaseous precursor source in the

162   experiments, from which the flow rate of 1,3,5-TMB/N_2 varied between 1 – 3 sccm (standard

163   cubic centimeter per minute), leading to $7.08 \times 10^{11} – 1.54 \times 10^{12}$ molecule cm^{-3} of 1,3,5-TMB in

164   the 1st-round experiments, and 7.55×10^{11} or 8.45×10^{11} molecule cm^{-3} of 1,3,5-TMB in the 2nd-

165   round experiments, respectively (Table S1). A total flow of 15 slpm (standard liters per minute)

166   zero-gas generated by a zero-gas generator (model 737-13, Aadco Instruments Inc.), together

167   with the 1,3,5-TMB/N_2 flow, was introduced into the OFR. The reaction time in both series of

168   experiments was kept at around 53 s and the flow reactor was kept as a plug flow one in both

169   series. The flow in the PAM OFR is laminar with a very low axial mixing, as characterized

170   with a Taylor dispersion model in a previous study (Lambe et al., 2011). 6 slpm out of the 15

171   slpm zero-gas was initially passed through a Nafion humidifier (Perma Pure Model FC100-80-

172   6MSS) filled with ultra-pure water and finally converged with the main flow into the OFR to

173   achieve and keep a desired RH of 20.0 ± 2.5 % in the OFR throughout all the experiments, and

174 2 slpm was initially passed through a separate ozone chamber, resulting in an initial ozone

175 concentration of around $1.05\times10^{13} - 2.16\times10^{13}$ molecule cm^{-3} in the OFR in the 1st-round

176 experiments and $3.01\times10^{12} - 3.72\times10^{12}$ molecule cm^{-3} in the 2nd-round experiments,

177 respectively. The OFR was operated with only the 254 nm lights on, under which the primary

178 oxidant production reactions in the OFR were $O_3 + hv\ (254\ nm) \rightarrow O_2 + O(^1D)$ and

179 $O(^1D) + H_2O \rightarrow 2OH$. After turning on of UV lights, a HOM compound is believed to be

180 generated if its signal is more than 3 standard deviations of its background signal. If the

181 fluctuations in the 1-min-averaged signals of both TMB in the Vocus PTR and typical HOMs

182 (i.e., $C_9H_{14}O_7(NO_3)^-$) in the nitrate CIMS are within 2% during a 10-min period, a steady state

183 was assumed to be reached. It usually took around no more than 2 minutes for the signals of

184 HOMs to stabilize after the adjustment of UV lights. We typically monitored the reaction

185 products for around 20 minutes for each experiment. An ozone monitor (Model 106-M, 2B

186 technologies) and a trace-gas analyzer for NO-NO$_2$-NO$_x$ (Thermo, 42i-TL) were placed at the

187 exit of the OFR to measure concentrations of ozone and NO$_x$, respectively.

188   Non-tropospheric VOC and OVOC photolysis is a typical issue that should be taken into

189 account when evaluating the OFR settings, especially under the high UV light dose settings in

190 the 1st-round experiments. Our evaluation on photolysis of the precursor and HOMs shows that

191 photolysis was not a contributor to our observation on C9 and C18 HOM formation. The

192 photolysis rate of 1,3,5-TMB can be estimated based on the absorption cross-sections of 1,3,5-

193 TMB at 254 nm (Keller-Rudek et al., 2013) and UV photon fluxes estimated by a chemistry

194 model discussed in the following sections. The ratio of photolysis-to-OH reaction for 1,3,5-

195 TMB in our 1st-round experiments was merely $0.010 - 0.033$. Hence, photolysis of 1,3,5-TMB

196 was insignificant in the OFR. For stabilized products such as C9 and C18 HOMs, the cross

197 sections of organic molecules are usually $\sim 3.9\times10^{-18} - 3.9\times10^{-17}$ cm^2 (Peng et al., 2016), while

198 the reaction rate between OH and the stabilized first-generation products are estimated to be

199 around 1.28×10^{-10} molecule^{-1} cm^3 s^{-1}, as suggested by Master Chemical Mechanism (MCM)

200 (Jenkin et al., 2003). Hence, the ratio of photolysis rates of C9 and C18 HOMs to their

201 secondary OH oxidation rates is estimated to be around $0.020 - 0.056$ in the 1st-round

202 experiments. In the 2nd-round, the influences of photolysis should be even lower due to the

203 much lower light intensity.

204   For experiments with NO$_x$ in the 1st-round experiments, 350 sccm N$_2$O (99.999%, Air

205 Liquid) was added into the OFR to produce and sustain NO$_x$ mixing ratios at levels that were

206 sufficiently high to be a competitive sink for RO$_2$ radicals. NO and NO$_2$ were produced via the

207 reaction $N_2O + O(^1D) \rightarrow 2NO$, followed by the reaction $NO + O_3 \rightarrow NO_2 + O_2$. Two sets of

208 irradiance intensities were chosen for NO$_x$ experiments, generally resulting in two NO$_x$ levels,

209   4.41×10^{10} molecule cm^{-3} NO + 1.72×10^{12} molecule cm^{-3} NO$_2$ (Exp. 1-41 – 1-54) and 1.18×10^{11}

210   molecule cm^{-3} NO + 2.94×10^{12} molecule cm^{-3} NO$_2$ (Exp. 1-55 – 1-68) at the exit of the OFR.

211   With the aim to slightly modify OH exposure but keep NO$_x$ concentrations constant among

212   each set of experiments, the initial concentrations of 1,3,5-TMB were adjusted in a large range

213   from 4.09×10^{11} to 2.06×10^{12} molecule cm^{-3} while RH and irradiances were not changed, as an

214   increase in the precursor concentration corresponds to a larger sink for OH. In the 2nd-round

215   experiments, due to the lower O(^{1}D) in the PAM OFR, 2.5 slpm pure N$_2$O was utilized instead,

216   whereas the total flow rate was kept the same as that in the 1st-round. We lowered the light

217   intensity to obtain a lower [OH] in the PAM OFR, which also resulted in fluctuations in the NO

218   concentrations ([NO]) from 3.19×10^{10} to 1.74×10^{11} molecule cm^{-3} and the NO$_2$ concentrations

219   ([NO$_2$]) from 2.70×10^{11} to 9.31×10^{11} molecule cm^{-3}.

220   A nitrate CIMS (Ehn et al., 2014; Eisele and Tanner, 1993) and a Vocus PTR (Krechmer

221   et al., 2018) were deployed at the exit of the OFR to measure the oxidation products of 1,3,5-

222   TMB in the 1st-round experiments. These two mass spectrometers have been well characterized

223   in a previous study (Wang et al., 2020b).

224   The sample flow rate for the nitrate CIMS in the 1st round-experiments was 8 slpm through

225   a Teflon tube with an outer diameter (OD) of 1/4 in. and a length of 70 cm. The sheath flow for

226   the nitrate CIMS was supplied by a zero-gas generator at a flow rate of 15 slpm. Mass resolution

227   was approximately 8000 for ions with m/z larger than 200 Th. HOMs generated from TMB

228   oxidation were charged in the ambient pressure interface region by collisions with nitrate

229   clusters, $(HNO_3)_x\cdot NO_3^-$ ($x = 0 - 2$), and detected by nitrate CIMS as clusters with NO$_3^-$, i.e.,

230   HOM$\cdot$NO$_3^-$ (Hyttinen et al., 2015). In addition, HOMs' signals were corrected with relative

231   transmission efficiencies of our nitrate CIMS (Heinritzi et al., 2016). We followed the same

232   sampling method of PAM OFR as those in previous studies, in order to obtain a similar flow

233   tube residence time distributions (RTDs) and thus validate usage of a modified PAM_chem_v8

234   model to estimate concentrations of radicals in the OFR as discussed below.

235   Vocus PTR was applied to quantify precursor concentrations. The focusing ion-molecule

236   reactor (FIMR) was heated up and its temperature was maintained at 100 ℃ during the

237   experiments. The FIMR can be operated under 2.0 mbar without a strong interference from

238   corresponding water clusters when ionizing the neutral compounds. The Vocus front and back

239   voltages were 650 V and 15 V, respectively, forming an axial voltage of 635V and a reduced

240   electrical field (*E/N*, where E is the electric field strength and N is the number density of the

241   buffer gas in FIMR) of 180 Td. The radio frequency (RF) voltages and frequency were set to

242   be 450 V and 1.3 MHz, respectively. The sample flow was introduced to the Vocus PTR

243   through a Teflon tube with an OD of 1/4 in. and a length of 120 cm from the OFR. A total

244   sample flow of 1.4 slpm was maintained by a pump with an orifice to minimize the delay time

245   of sampling, from which approximately 125 sccm was sampled into the FIMR through a
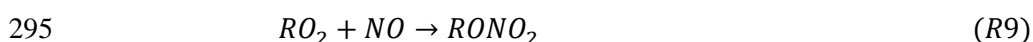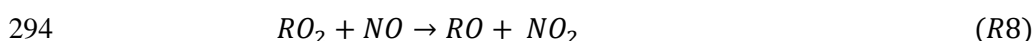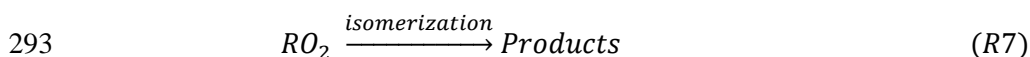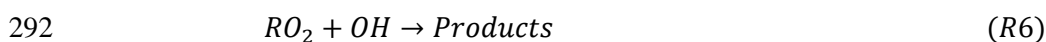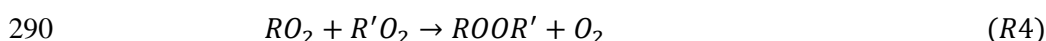
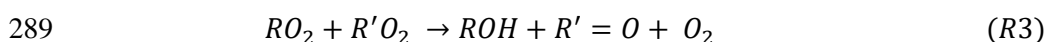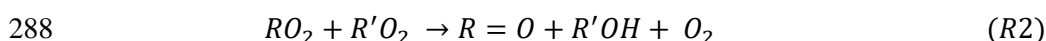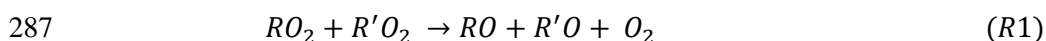246   capillary tube.

247   In the 2nd-round experiments, a Vocus CI-TOF (Towerk AG, Switzerland) equipped with

248   a Vocus Aim inlet and the same nitrate-ion chemical ionization source as adopted in the 1st-

249   round experiments was utilized to measure oxidation products, hereafter referred as nitrate CI-

250   TOF. The nitrate CI-TOF was characterized with a flat transmission efficiency between m/z 60

251   Th and m/z 500 Th, as well as a mass resolution of 10000 at m/z 200 Th. In this series of

252   experiments, the reaction products were sampled from the PAM OFR via a 30 cm-long Teflon

253   tube with a 1/2 in. OD to our nitrate CI-TOF. The Vocus PTR and the ozone monitor were

254   connected to the PAM OFR from a separate port via a 120 cm-long Teflon tube with a 1/4 in.

255   OD.

256   We did not quantify HOMs' concentrations. Since the inner diameters of PAM OFR,

257   sampling tube, and the nitrate CIMS inlet were different, and two reducing unions were used

258   during sampling, the estimation of the penetration efficiency and sampling efficiency of HOMs

259   are thus of a significant uncertainty. The initial concentrations of TMB utilized in both sets of

260   experiments fluctuated slightly, which resulted from sample preparation processes and were

261   more obvious in the 1st-round experiments. Therefore, in the discussion on the data of the 1st-

262   round experiments, we tried to minimize potential influences of the differences in the initial

263   TMB concentrations on the signals of HOMs by normalizing the HOMs signals with the initial

264   TMB signal. To precisely illustrate changes in the abundance of HOMs at different OH

265   exposures, a normalized signal was chosen to present the abundance of detected HOMs, which

266   is defined as the ratio of the signals of HOMs in the nitrate CIMS normalized by the reagent

267   ions and the initial signal of 1,3,5-TMB, i.e., $S(HOMs)/S(TMB)$. $S(HOMs)$ is the signal of

268   HOM detected by the nitrate CIMS normalized with the signal of reagent ions, whereas

269    $S(TMB)$ is the initial signal of 1,3,5-TMB detected by the Vocus PTR.

270   To compare chemical regimes of two series of experiments and the ambient atmosphere,

271   a PAM chemistry model (PAM_chem_v8), utilized widely in previous studies, were chosen

272   with the latest updates to calculate radical profiles in our OFR (Li et al., 2015; Cheng et al.,

273   2021; Wang et al., 2020b; Mehra et al., 2020; Lambe et al., 2015, 2018; Peng and Jimenez,

274   2020; Lambe et al., 2017). This model is based on a photochemical box model that includes

275   chemistry of photolysis of oxygen, water vapor, and other trace gases by the primary

276   wavelengths of mercury lamps, and simplified VOC and RO_2 chemistry, but further reactions

277   of the first-generation stabilized products and the second-generation organic radicals are not

278   considered. The reactions and corresponding kinetics utilized in this model were summarized

279   in Table S2. In this work, autoxidation and accretion of 1,3,5-TMB-derived BPR, as well as

280   subsequent reactions of the autoxidation product of BPR, i.e., $C_9H_{13}O_7\cdot$, are newly implemented

281   or modified in this model (Reaction No. 46 – 62 in Table S2). These two radicals were the most

282   significant RO_2 in the system and represented the whole RO_2 pool in the PAM chemistry model

283   simulation. The pathways of peroxy radicals and their kinetics are discussed below. NO_x-related

284   reactions are also included in the model. When experiments without NO_x are simulated, these

285   NO_x-related reactions do not contribute to the simulation results.

286   The detailed reactions involved with RO_2 include:

287    $$RO_2 + R'O_2 \rightarrow RO + R'O + O_2 \quad\quad\quad (R1)$$

288    $$RO_2 + R'O_2 \rightarrow R=O + R'OH + O_2 \quad\quad\quad (R2)$$

289    $$RO_2 + R'O_2 \rightarrow ROH + R'=O + O_2 \quad\quad\quad (R3)$$

290    $$RO_2 + R'O_2 \rightarrow ROOR' + O_2 \quad\quad\quad (R4)$$

291    $$RO_2 + HO_2 \rightarrow ROOH + O_2 \quad\quad\quad (R5)$$

292    $$RO_2 + OH \rightarrow Products \quad\quad\quad (R6)$$

293    $$RO_2 \xrightarrow{isomerization} Products \quad\quad\quad (R7)$$

294    $$RO_2 + NO \rightarrow RO + NO_2 \quad\quad\quad (R8)$$

295    $$RO_2 + NO \rightarrow RONO_2 \quad\quad\quad (R9)$$

296    $$RO_2 \rightarrow physical\ loss \quad\quad\quad (R10)$$
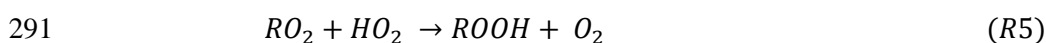
297    $R1$, $R2$, and $R3$ are reactions of $RO_2 + RO_2$, forming alkoxy radicals, carbonyl termination

298   products, and hydroxyl termination products, respectively. $R4$ is the accretion reaction,

299   forming dimers via combination of two monomeric RO_2. $R5$ is the reaction between RO_2 and

300   HO_2, forming hydroperoxyl radicals. The reaction rate constants for RO_2 in $R1 – R5$ are

301   obtained by MCM or previous investigations (e.g., Jenkin et al., 2003; Berndt et al., 2018; Peng

302   and Jimenez, 2020). We treat $R1 – R3$ as a total reaction with a reaction rate constant of 8.8×10^{-13}

303   molecule^{-1} cm^3 s^{-1}, and branching ratios of $R1 - R3$ of 0.6, 0.2, and 0.2, respectively, as

304   suggested by MCM (Jenkin et al., 2003). The reaction rate constants of BPR and $C_9H_{13}O_7\cdot$ for

305    $R4$ are 1.7×10^{-10} and 2.6×10^{-10} molecule^{-1} cm^3 s^{-1}, respectively (Berndt et al., 2018b). The

306   reaction rate constants for $R5$ is 1.5×10^{-11} molecule^{-1} cm^3 s^{-1} (Jenkin et al., 2003).

307        $R6$ is the reaction between OH and RO_2, whose reaction rate constant is 1×10^{-10} molecule^{-1}

308   cm^3 s^{-1} according to previous studies (Bossolasco et al., 2014; Yan et al., 2016; Assaf et al.,

309   2016, 2017; Peng and Jimenez, 2020). Current knowledge on the reaction products for the

310   reaction of $CH_3O_2\cdot + OH$, the most studied $RO_2 + OH$ reaction, is summarized in Table S3. The

311   products of this reaction are suggested to include a Criegee intermediate ($CH_2O_2\cdot$), a stabilized

312   methylhydrotrioxide (CH_3OOOH), an alkoxy radical ($CH_3O\cdot$), and methanol (CH_3OH) (Yan et

313   al., 2016; Fittschen, 2019; Caravan et al., 2018; Müller et al., 2016). Müller et al. (2016) and

314   Caravan et al. (2018) suggested that the formation of $CH_2O_2\cdot$ is actually infeasible, and Yan et

315   al. (2016) estimated an upper limit branching ratio of 5% for this pathway. The branching ratios

316   of stabilized products CH_3OH and CH_3OOOH are 6 – 7% (Caravan et al., 2018; Müller et al.,

317   2016) and 7% (Müller et al., 2016), respectively. The most significant product of this reaction

318   is the alkoxy radical ($CH_3O\cdot$), with a branching ratio of more than 86% (Müller et al., 2016).

319   In the absence of NO_x, CH_3OH and $CH_3O\cdot$ can also be formed via the traditional unimolecular

320   reaction between $CH_3O_2\cdot$ and RO_2, i.e., $R1$ and $R3$. The possible role of this reaction of large

321   RO_2, i.e., BPR and other C9-RO_2, with OH has not yet been investigated. However, according

322   to the branching ratios for the reaction of $CH_3O_2\cdot$ + OH, this reaction is likely to form RO

323   instead of stabilized C9 products. Hence, we assume that the branching ratios of hydrotrioxide

324   (ROOOH), RO, and ROH are 0.07, 0.86, and 0.07, respectively, for BPR + OH and C9-RO_2 +

325   OH.

326       $R7$ is the unimolecular reactions of RO_2 in the PAM OFR. RO_2 isomerization rate

327   coefficients are highly dependent on their structures, spanning from $10^{-3} – 10^6$ s^{-1} (Bianchi et

328   al., 2019; Crounse et al., 2013; Knap and Jørgensen, 2017; Praske et al., 2018). However, only

329   some substituted acyl RO_2 can undergo rapid isomerization at a reaction rate of 10^6 s^{-1} (Knap

330   and Jørgensen, 2017). 1,3,5-TMB-derived BPR and its autoxidation product, $C_9H_{13}O_7\cdot$, do not

331   belong to this group of substituted acyl RO_2 (Molteni et al., 2018; Tsiligiannis et al., 2019). The

332   most important unimolecular reactions for 1,3,5-TMB-derived BPR is likely autoxidation while

333   the precise autoxidation reaction rates of 1,3,5-TMB-derived BPR and other RO_2 in this system

334   are currently unclear (Bianchi et al., 2019; Molteni et al., 2018). Previous theoretical

335   investigations suggest that more than 90% BPR generated by the oxidation of 1,3,5-TMB

336   possess a structure favoring autoxidation and thus their overall autoxidation reaction rate is

337   relatively fast (Wang et al., 2017). We follow quantum calculation results on the autoxidation

338   reaction of a methyl group adjacent to the RO_2 functionality group (Wang et al. 2017), and time

339   the suggested rate (0.026 s^{-1}) by 3 due to the symmetry with three methyl groups in our parent

340   compound. The obtained autoxidation reaction rate is 0.078 s^{-1}.

341       $R8$ and $R9$ are the reactions between NO and RO_2, generating alkoxy radicals and

342   organonitrates, respectively. The reaction rate for the sum of these two reactions is 8.5×10^{-12}

343   molecule^{-1} cm^3 s^{-1}. The branching ratios of these two reactions are 0.843 and 0.157, respectively,

344   according to MCM (Jenkin et al., 2003).

345   Alkoxy radicals, RO, will be generated in $R1$, $R6$, and $R8$. The widely used near-explicit

346   mechanism, MCM, assumes that RO formed via the alkoxy channel of BPR ($R1$) will

347   decompose into small molecules. Recently, Xu et al. (2020) probed the chemical fates of BPR-

348   derived RO, hereafter referred to as bicyclic alkoxy radical (BCP-oxy), in the oxidation of

349 benzene by laboratory experiments and model calculations, which can be taken as a reference
350 to induce the mechanism of 135-TMB-derived BCP-oxy. BCP-oxy can undergo two reactions,
351 i.e., ring-breakage and ring-closure, and a new calculation result suggests that the branching
352 ratio of ring-breakage reaction is larger than 98% (Wang et al., 2013). 56% of ring-breakage
353 reactions will break benzene-derived BCP-oxy into butenedial and glyoxal, and the rest 44%
354 will generate a C6 alkyl radical by a 1,5-aldehydic H-shift. The latter C6 alkyl radical will
355 further undergo other reactions, including a 93% branching ratio for decomposition reactions
356 that results in a reduction of carbon atom number (Xu et al., 2020). Therefore, most of benzene-
357 derived BCP-oxy will likely decompose into compounds with fewer carbon atoms. We assume
358 that 1,3,5-TMB-derived BCP-oxy will undertake these decomposition reactions with a similar
359 branching ratio, which means that these radicals cannot form a large number of stabilized
360 products that can influence the distributions of stabilized C9 products in nitrate CIMS.

361      $R10$ is the physical loss of RO_2. The physical loss of RO_2 in the PAM OFR consists of the
362 condensation loss to the aerosol particles and the diffusion loss to the OFR walls. In our
363 experiments, measurement results by a long-SMPS show that the aerosol particles presented in
364 the PAM OFR were few. The long SMPS consisted of a long-DMA (TSI model 3081) and a
365 CPC (TSI model 3787), covering a particle number size distribution from 13.6 nm to 736.5 nm.
366 Thus, though not detected in this study, we cannot absolutely deny the possibility that particles
367 might have been generated, resulting in a larger physical loss of HOMs. This part of physical
368 loss might be underestimated. The first-order loss rate of HOMs to the OFR walls, k_{wall}, is
369 limited by eddy diffusion and can be calculated with the following function (Cheng et al., 2021;
370 Palm et al., 2016; McMurry and Grosjean, 1985):

371 $$k_{wall} = \frac{A}{V} \cdot \frac{2}{\pi} \cdot \sqrt{k_e D_g} \qquad\qquad (Eq1)$$

372 where the OFR surface-area-volume ratio (A/V) is 25 m^{-1} and the coefficient of eddy diffusion
373 (k_e) is 0.0042 s^{-1}, as estimated by the method utilized in a previous study (Brune, 2019) and
374 given in $Eq2$.

375 $$k_e = 0.004 + 10^{-2.25} V^{0.74} \qquad\qquad (Eq2)$$

376 where V is the enclosure volume (m^3). The molecular diffusion coefficient, D_g, is estimated
377 with the method as described by Fuller et al. (1966) and is around 5×10^{-6} m^2 s^{-1} with 1,3,5-TMB
378 derived BPR as an example. Hence, k_{wall} is around 0.0023 s^{-1} in the PAM OFR.

379   Other kinetic data in the modified PAM_chem_v8 model are obtained from the IUPAC
380 (International Union of Pure and Applied Chemistry) dataset (https://iupac-aeris.ipsl.fr, last
381 access: 26 October 2023) and the MCM dataset (MCM v3.3.1, https://mcm.york.ac.uk/MCM/,
382 last access: 9 October 2023).

383   For the 1st-round experiments, the input parameters of temperature, mean residence time,
384   water vapor concentration, O_3 concentration, and the initial 1,3,5-TMB concentration are 25 °C,
385   53 s, 0.63%, 1.23×10^{13} molecule cm^{-3}, and 1.23×10^{12} molecule cm^{-3}, respectively, as measured
386   directly. For the 2nd-round experiments, the input parameters of O_3 concentration and the initial
387   1,3,5-TMB concentration were updated as 3.68×10^{12} molecule cm^{-3} and 7.55×10^{11} molecule
388   cm^{-3}, respectively. In the NO_x experiments, the input flow rate of N_2O is 350 sccm in the 1st-
389   round experiments and 2.5 slpm in the 2nd-round experiments, respectively. The actinic flux at
390   254 nm, I_{254}, is constrained by comparing OH exposures by model output and OH exposures
391   estimated by the consumption of 1,3,5-TMB as measured by the Vocus PTR. Consumption of
392   O_3 estimated by the model agrees well with the measured results, with discrepancies being
393   always within 10% at different OH exposures.

394   **3 Results and discussion**

395   **3.1 Comparison of chemical regimes**

396   Concentration profiles of OH, RO_2, and HO_2 as a function of OH exposures in our high
397   [OH] experiments without NO_x, i.e., the 1st-round experiments, are illustrated in Figure S1a.
398   According to the modified PAM_chem_v8 model, when [OH] increased from 9.32×10^7 to
399   1.03×10^9 molecule cm^{-3}, $[HO_2]$ increased from 7.25×10^8 to 2.79×10^9 molecule cm^{-3}, whereas
400    $[RO_2]$ concentrations increased from 5.17×10^9 to 9.5×10^9 molecule cm^{-3}. The radical
401   concentrations in high [OH] experiments with NO_x (Figure S1b) varied in a similar range, with
402    $[RO_2]$ ranging from 4.38×10^9 to 9.13×10^9 molecule cm^{-3}, HO_2 ranging from 4.47×10^9 to
403   6.47×10^9 molecule cm^{-3}, and OH ranging from 3.86×10^8 to 7.82×10^8 molecule cm^{-3},
404   respectively. The ratios of between HO_2/OH and RO_2/OH in the 1st-round experiments were
405   generally in the same order of magnitude as those in with the ambient atmosphere (Whalley et
406   al., 2021).

407   Radical concentrations were also estimated by the PAM_chem_v8 model to illustrate the
408   chemical regimes in the 2nd-round experiments (Table S4). The average $[HO_2]$, [OH], and $[RO_2]$
409   were 9.7×10^7, 1.64×10^7, and 1.69×10^9 molecule cm^{-3}, respectively, in Exp. 2-3, and were
410   6.7×10^7, 1.04×10^7, and 1.34×10^9 molecule cm^{-3}, respectively, in Exp. 2-4, both of which
411   generally differ by no more than a factor of 3 from the summer daytime ambient ones in polluted
412   atmospheres (Tan et al., 2017, 2018, 2019; Whalley et al., 2021; Lu et al., 2012). The average
413    $[HO_2]$, [OH], and $[RO_2]$, as well as the NO and NO_2 concentrations in Exp. 2-7 are generally
414   very close to those in the same environment (Tan et al., 2019).

415   We take Exp. 1-12 ([OH] = $\sim8.47\times10^8$ molecule cm^{-3} and $NO_x = 0$) and Exp. 2-3 ([OH] =
416    $\sim1.64\times10^7$ molecule cm^{-3} and $NO_x = 0$) as representative examples and compare simulation

417   results with those from the ambient atmosphere, since NO_x in the ambient is believed not to

418   impact relative ratios for $R1 - R3$, $R5$, and $R6$. In the ambient atmosphere, the average $[HO_2]$,

419   [OH], and $[RO_2]$ were 2.7×10^8, 8.0×10^6, and 1.4×10^9 molecule cm^{-3}, respectively, around

420   summertime noon in urban Beijing (Whalley et al. 2021), and $(4 - 28)\times10^8$, $(0.8 - 2.4)\times10^7$,

421   and 1.2×10^9 molecule cm^{-3} (modeled) at a suburban site in Yangtze River Delta (Ma et al. 2022).

422   As shown in Figure 1a, for the most important RO_2, BPR, the fractions of monomeric

423   termination reactions of $RO_2 + RO_2$ ($R1 - R3$), $RO_2 + HO_2$ ($R5$), and $RO_2 + OH$ ($R6$) were

424   6.2%, 29.3%, and 64.5%, respectively, in Exp.1-12. In contrast, the fractions were 32.5%,

425   31.8%, and 35.7%, respectively, in Exp. 2-3, whereas the values were 20.3%, 66.6%, and 13.2%,

426   respectively, for summertime, urban Beijing.

427   **(a)**
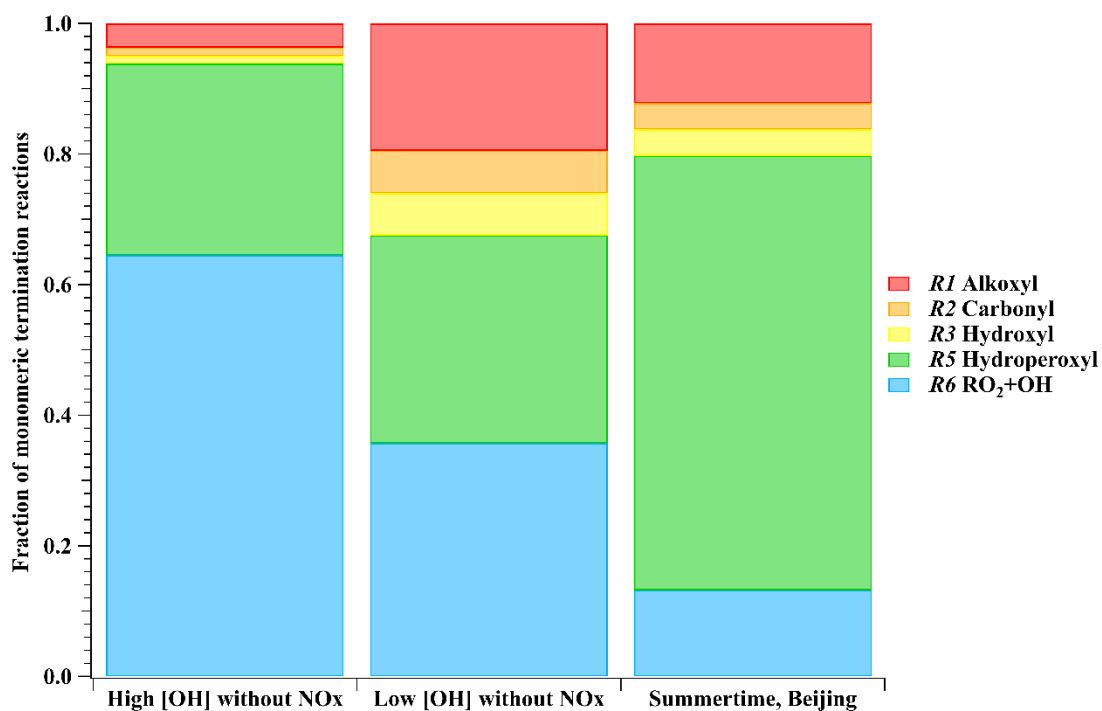
428

429   **(b)**

430

431   **(c)**

432

14
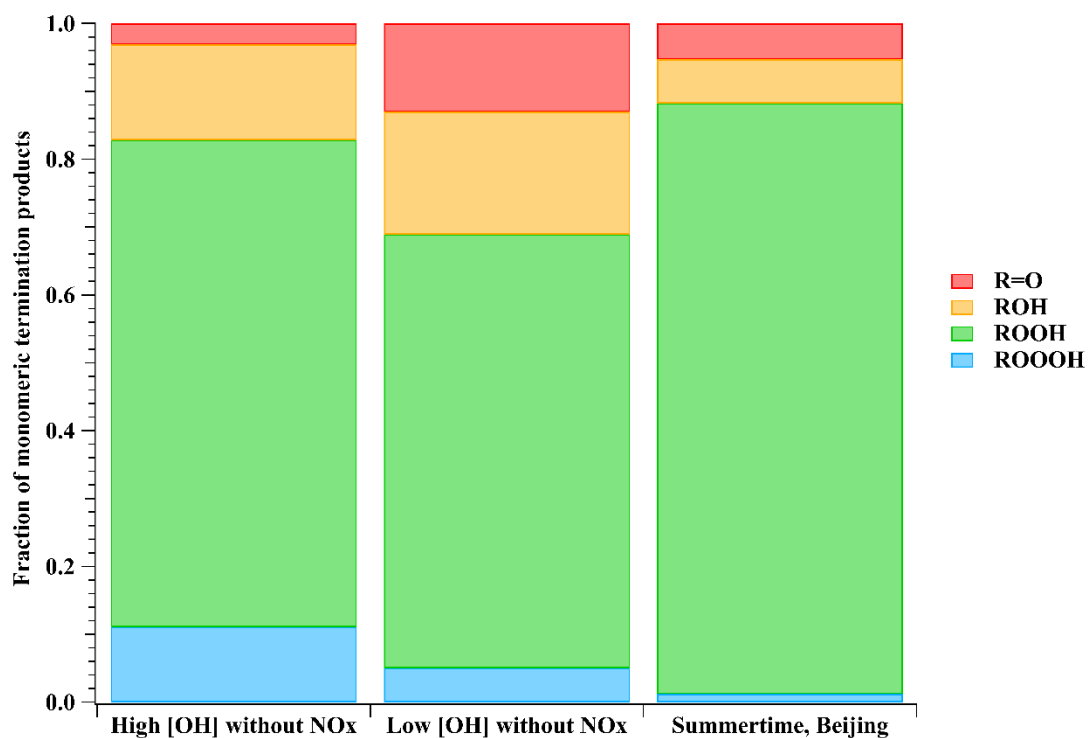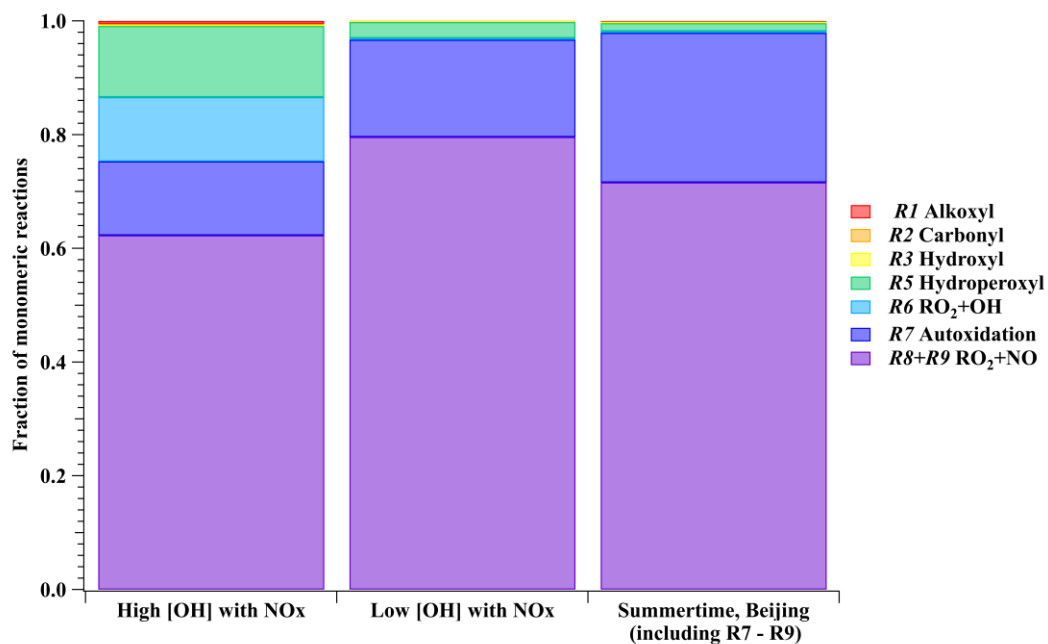
433   **(d)**
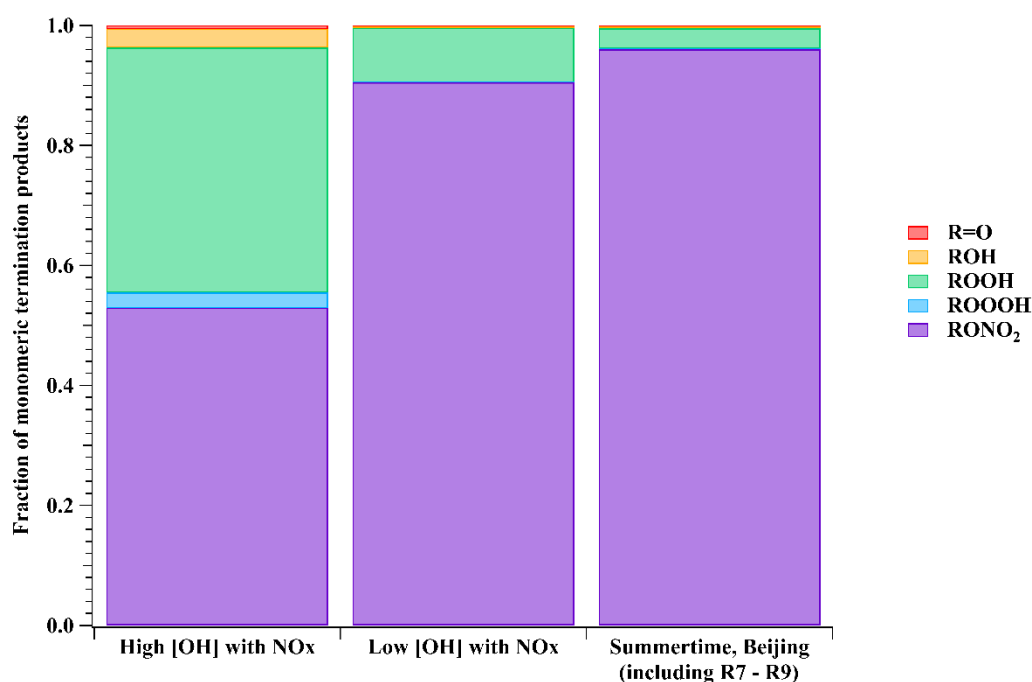
434

435   **Figure 1.** (a) The fraction of monomeric termination reactions and (b) monomeric termination
436   products of BPR in a representative high [OH] experiment without NO_x (Exp. 1-12), a
437   representative low [OH] experiment without NO_x (Exp. 2-3), and summertime, urban Beijing
438   (Whalley et al. 2021). NO_x related reactions and products for the Beijing study are not included
439   for a better comparison. (c) The fraction of monomeric reactions (R1 – R3 and R5 – R9) and
440   (d) monomeric termination products of BPR in a representative high [OH] experiment with
441   NO_x (Exp. 1-48), a representative low [OH] experiment with NO_x (Exp. 2-7), and summertime,
442   urban Beijing (Whalley et al. 2021). Reactions and kinetic rate coefficients used in the
443   calculations are provided in Table S2.

444   Our NO_x-free experiments are characterized with an inherent drawback that the proportion
445   of the HO_2 termination pathway ($R5$) is actually lower than that under ambient conditions,
446   which is similar to most other laboratory experiments (Bianchi et al., 2019). In our high [OH]
447   experiments without NO_x, the reaction rates of unimolecular reactions, e.g., autoxidation
448   reaction ($R7$) and condensation ($R10$) did not change with [OH] that increased in our
449   experiments relative to that in the ambient. As a result, relative proportions of autoxidation and
450   condensation were lowered. On the other hand, 1,3,5-TMB-derived BPR was suggested to
451   undergo autoxidation ($R7$) at a reaction rate of 0.078 s^{-1} (Wang et al., 2017), which represented
452   36.8%, 94.4%, and 92.8% of the overall rates of $R1 – R3$ and $R5 – R7$ in Exp. 1-12, Exp. 2-3,
453   and summertime, urban Beijing, respectively. Because of its dominant proportion in Exp. 2-3
454   and the ambient, the autoxidation channel is not included for clarity in Figure 1a. Autoxidation

did possess a lower significance in our high [OH] experiments due to the other accelerated bimolecular reactions. However, it would only influence the oxygen content of our products but would not change the DBE. Both accretion reaction ($R4$) and condensation ($R10$) have been taken into account in the model, but they would not influence the distributions of monomeric stabilized products. We will specifically discuss these two pathways in the following sections because of their complexity between the laboratory and ambient conditions.

RO$_2$ other than BPR and $C_9H_{13}O_7\cdot$ existed in the PAM OFR, which were not included in the model simulation. Their reaction rates of the accretion reaction ($R4$) and the autoxidation reaction ($R7$) should be different from BPR and $C_9H_{13}O_7\cdot$ due to the strong dependence of these two reaction rates on the molecular structure. Rates for the other reaction channels, on the other hand, should be the same as those of BPR and $C_9H_{13}O_7\cdot$. Therefore, their fates in terms of the monomeric termination reactions ($R1 - R3$, $R5 - R6$, and $R8 - R9$) should be similar as BPR and $C_9H_{13}O_7\cdot$.

Calculated from yields of stabilized monomeric termination products of BPR, the fractions of monomeric termination reaction products in Exp. 1-12, Exp. 2-3, and summertime, urban Beijing (Whalley et al. 2021) are presented in Figure 1b, showing a lot of similarities between these conditions. The fractions of R=O, ROH, ROOH, and ROOOH in Exp. 1-12 were 3.1%, 14.1%, 71.7%, and 11.1%, respectively. These fractions were 13.0%, 18.1%, 63.9%, and 5.0%, respectively, in the Exp. 2-3, and were 5.3%, 6.5%, 87.0%, and 1.2%, respectively, in the summertime Beijing case. Among them, the majority of products are always ROOH and ROH, with ROOH being the most abundant. Therefore, the monomeric termination products of BPR in our experiments are atmospheric relevant. In addition, only the R=O product has a DBE higher than the reacted RO$_2$, but merely accounted for a limited proportion. All the other stabilized termination products have a DBE that is 1 lower than the precursor, and are the majority in both laboratory and ambient conditions. This indicates that the majority of the first-generation products typically have a DBE that is 1 lower than that of 1,3,5-TMB, whereas the majority of subsequent-generation products typically have a DBE that is 2 lower than that of 1,3,5-TMB. Once a monomeric compound with a DBE that is at least 2 lower than that of 1,3,5-TMB was observed, multi-generation OH reactions have happened in the system.

In laboratory experiments in absence of NO$_x$ (e.g., Exp.1-12), the proportions of $R8 - R9$, i.e., the NO channel in the urban atmosphere were attributed to termination reactions of $R1 - R6$, i.e., RO$_2$ + RO$_2$, accretion reaction, RO$_2$ + HO$_2$, and RO$_2$ + OH. By expanding proportions of these termination reactions, laboratory investigations on product distributions can be facilitated, as the detection of certain HOM products became more precise and the mass spectra became simplified.

490   In experiments with NO_x, the chemical fates of BPR in high [OH] experiments (Exp. 1-48

491   as an example, [OH] = ~6.77×10^8 molecule cm^{-3}, NO = ~4.73×10^{10} molecule cm^{-3}. NO_2 =

492   ~1.67×10^{12} molecule cm^{-3}), low [OH] experiments (Exp. 2-7 as an example, [OH] = ~1.69×10^7

493   molecule cm^{-3}, NO = ~3.19×10^{10} molecule cm^{-3}. NO_2 = ~2.70×10^{11} molecule cm^{-3}), and the

494   summertime, urban Beijing are compared. As shown in Figure 1c, in all three conditions, RO_2

495   reactions with NO were always the most significant pathway, with autoxidation being the

496   second most significant.

497   Accounting for at least 52% of monomeric termination products under all conditions,

498   organonitrates were always the most important termination products, as shown in Figure 1d.

499   On the other hand, based on the formulae of organonitrates, the detailed formulae of monomer

500   RO_2 could be probed, which can help us better understand the chemical reactions inside the

501   system. Alkoxy radicals generated in the NO termination channel will unlikely influence the

502   distributions of C9 stabilized products since they tend to get decomposed in the subsequent

503   reactions, as discussed in our previous discussion on the fate of alkoxy radicals in Section 2.

504   Due to the complexity of ambient RO_2 pool, it is difficult to estimate the detailed fraction

505   of accretion reactions $R4$. In the laboratory experiments, RO_2 pool mainly consists of BPR and

506   its autoxidation reaction product $C_9H_{13}O_7\cdot$, which both can undergo accretion reaction rapidly

507   (Berndt et al., 2018b). The concentrations of these two radicals were estimated by

508   PAM_chem_v8. The reaction rate of accretion ($R4$) for BPR was around 1.61 s^{-1} in Exp.1-12,

509   being 88.4% of $R1 - R7$, and was 0.29 s^{-1} in Exp.2-3, equivalent to 77.7% of $R1 - R7$.

510   Certain uncertainties exist in the estimation of the proportions of accretion reactions, as the

511   PAM_chem_v8 model only includes the first-generation reactions of precursors, whereas the

512   subsequential fragmentation and re-initiation of stabilized products can generate a series of new

513   RO_2 that will influence the proportions of accretion reactions. We are only certain that the

514   significance of accretion reactions in both Exp. 1-12 and Exp. 2-3 is larger than the ambient.

515   The much-expanded proportion of HOM dimers through accretion reactions makes it

516   inadequate to compare yields of HOM dimers and HOM monomers. However, this deviation

517   will not influence our conclusion on multi-generation OH oxidation and identification of HOM

518   dimers can help us identify the exact RO_2 in the OFR and confirm the conditions of secondary

519   OH oxidation according to the number of hydrogen atoms in the molecules.

520   In addition, certain compounds might have condensed onto pre-existing particles in the

521   real atmosphere before an appreciable fraction of such compounds undergoes the re-initiated

522   OH oxidation. Therefore, even if the same product can be generated both in the laboratory

523   experiments and the ambient atmosphere, the relative significance of this product is not

524   completely identical. Though OOMs might have the potential to undergo multi-generation OH

oxidation, the exact proportion of this reaction in the ambient strongly depends on their volatility, in other words, condensation sink of these OOMs. The typical monomeric termination products of 1,3,5-TMB-derived BPR, $C_9H_{12}O_4$, $C_9H_{14}O_4$, $C_9H_{14}O_5$, and $C_9H_{13}NO_6$, are estimated to have saturation vapor concentrations (C^*) of 30.20, 30.20, 0.85, and 3.39 $\mu g/m^3$ at 300 K, respectively with the volatility parameterization developed in the CLOUD chamber oxidation experiments of aromatics (Wang et al., 2020a). From the perspective of volatility, they all belong to semi-volatile organic compounds (SVOC, $0.3 < C^* < 300$ $\mu g/m^3$) and are expected to exist in both the condensed and the gas phases at equilibrium in the atmosphere (Bianchi et al., 2019). Compared to ambient conditions, the proportion of their condensation in the laboratory were biased to be lower due to the accelerated bimolecular reactions. However, this will not prevent the high [OH] experiments from showing the potential and ability of these compounds to go through re-initiated OH oxidation, as these compounds would exist in significant fractions in the gas phase in the real atmosphere.

However, the conditions are completely different for other HOM monomer products and HOM dimer products with much lower volatility. It is difficult for a HOM dimer, e.g., $C_{18}H_{26}O_{10}$ estimated with a C^* of 7.24×10^{-13} $\mu g/m^3$ at 300 K, to survive long enough to experience an appreciable re-initiated photochemical ageing. The lifetime of HOMs that can be classified as LVOCs ($3\times10^{-5} < C^* < 0.3$ $\mu g/m^3$) and ELVOCs ($C^* < 3\times10^{-5}$ $\mu g/m^3$) can be estimated according to the condensation sink (CS) in the atmosphere, as they are lost irreversibly onto surfaces. The median value of CS in urban Beijing was reported to be around 0.019 s^{-1} and 0.057 s^{-1} during NPF days and non-NPF days, respectively, whereas the values in Shanghai were reported to be around 0.013 s^{-1} and 0.017 s^{-1}. respectively (Deng et al., 2020; Yao et al., 2018), which are all much higher than the physical loss in our PAM OFR, i.e., 0.0023 s^{-1}. LVOCs and ELVOCs are believed to be lost irreversibly to the surface in both the laboratory and ambient because of their low volatility. By assuming a similar diffusion coefficient of LVOCs and ELVOCs to that of sulfuric acid, the lifetimes of LVOCs and ELVOCs in the ambient still can still be as high as 77 s for the condensation loss, which is close to the residence time of our PAM OFR. Therefore, if they were generated by oxidation of aromatics in the ambient, these LVOCs and ELVOCs should at least have the potential to experience the same OH exposures as those in our low [OH] experiments, i.e., at least 5.86×10^8 molecule cm^{-3} s. On the other hand, the detailed proportions of LVOCs and ELVOCs after a large OH exposure should be lower than those in the lab due to their magnified physical loss in the ambient. This means that if the multi-generation products of those compounds were observed in the ambient air, they should have been generated via a reaction that happened very recently.

**3.2 Oxidation products in high [OH] experiments**

560   A total of 33 HOM monomers with formulae of $C_{7-9}H_{8-16}O_{6-11}$ and 22 HOM dimers with

561   formulae of $C_{17-18}H_{24-30}O_{8-14}$ were observed in the 1st-round experiments of gas phase OH-

562   initiated oxidation of 1,3,5-TMB in the OFR, i.e., high [OH] experiments, as listed in Table S5.

563   The relative signal contributions of HOMs to the total signals of all HOMs at an OH exposure

564   of 2.38×10^{10} molecules cm^{-3} s are listed as an example in Table S5. The most abundant HOM

565   products were also shown in stack in Figure 2, whose relationships with OH exposures are

566   superimposed by a gamma function ($f(x) = ax^m e^{-x}$) simulation line to guide the eyes. The

567   sum of normalized HOM monomers' abundance increased monotonically up to the highest OH

568   exposure of 5×10^{10} molecule cm^{-3} s, whereas those of HOM dimers showed a non-monotonic

569   dependence on OH exposure. The observed faster increase of accretion products than that of

570   HOM monomers can be explained jointly by the fast second-order kinetics for accretion

571   reactions of RO$_2$ (Berndt et al., 2018b) and the high concentrations of relevant radicals in this

572   work. On the other hand, most of the first-generation HOM dimers formed from accretion

573   reactions contain at least one C=C bond and have more functionalities than HOM monomers,

574   and thus should be more reactive to OH radicals, which, together with a faster deposition loss

575   of dimers, results in a faster consumption of HOM dimers than monomers in the OFR. The

576   faster production and consumption of HOM dimers allowed their concentrations to summit at

577   middle levels of OH exposures. As stated in Section 3.1, because of the inherent disadvantage

578   of laboratory experiments, [RO$_2$] is always too high in the OFR, which has been pointed out in

579   a previous study (Bianchi et al., 2019). The accretion reactions in the OFR are relatively more

580   significant than it should be in the ambient atmosphere. We do not mean to compare the

581   abundance of HOM monomer and HOM dimer crossly here, but to pay attention to the

582   molecular characterization.

583 **(a)**
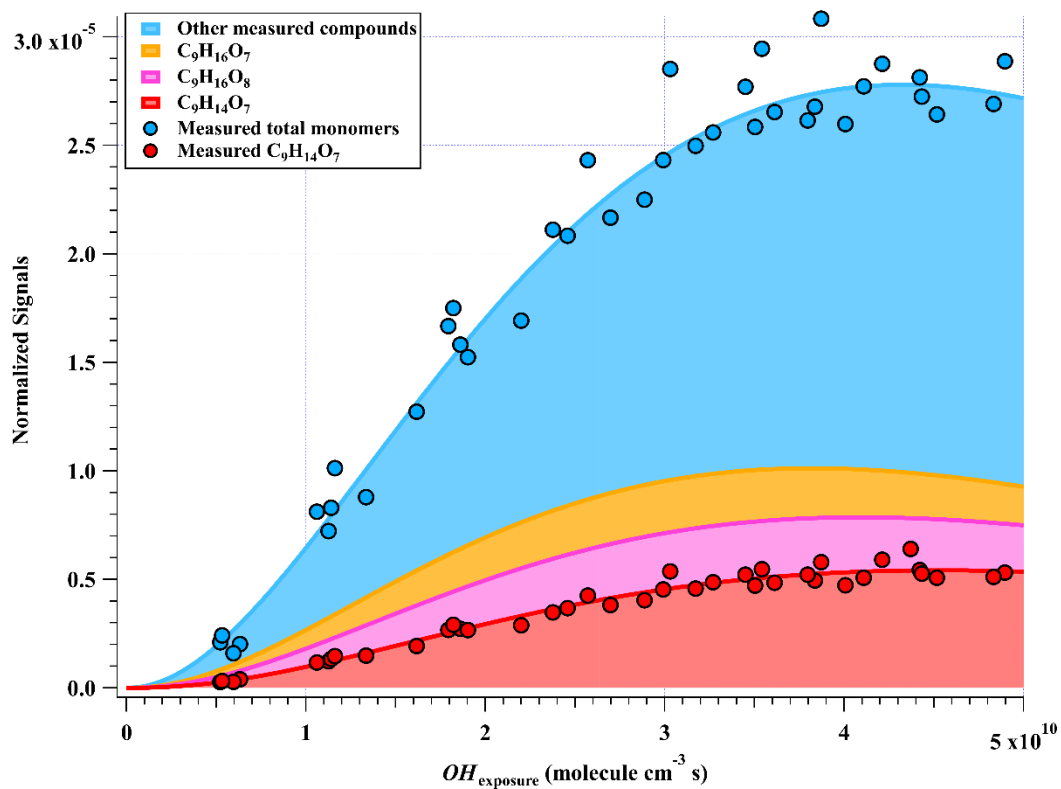
584

585 **(b)**
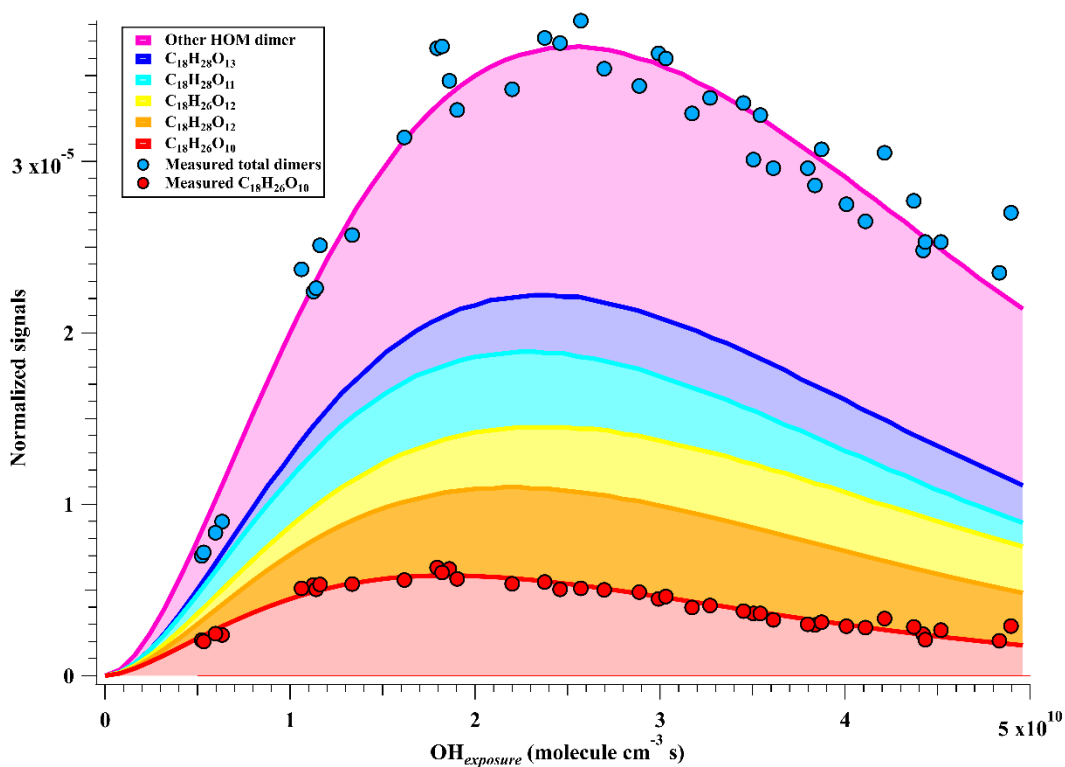
586

587 **Figure 2.** Normalized signals of (a) HOM monomers and (b) HOM dimers versus OH exposure

588 in the high [OH] experiments, which are fitted via a gamma function and shown in stack.

589   Theoretically, at a given RH and UV (i.e., a given [OH]), an increase in the initial TMB

590   would lead to formation of more RO_2, which corresponds to a larger RO_2/OH. However, under

591   our high [OH] experimental conditions, the $RO_2/OH/HO_2$ channels of RO_2 radicals are always

592   minor, and thus an increase in RO_2/OH would not have a significant impact on the relative

593   distribution of products formed from these channels. We compared product MS for experiments

594   with a similar OH exposure but different initial concentrations of TMB (e.g., Exp. 1-3 v.s. Exp.

595   1-19, and Exp. 1-12 v.s. Exp. 1-22). The OH exposures of Exp. 1-3 and Exp. 1-19 were

596   estimated by the consumption of precursors to be 5.2×10^9 and 5.3×10^9 molecule cm^{-3} s,

597   respectively, but the initial concentration of TMB of Exp. 1-3 was 25% more than that in Exp.

598   1-19. Meanwhile, the OH exposures of Exp. 1-12 and Exp. 1-22 were 4.5×10^{10} and 4.4×10^{10}

599   molecule cm^{-3} s, respectively, but the initial concentration of TMB of Exp. 1-12 was 48% more

600   than that in Exp. 1-22. Figure S2 shows comparisons between the product MS of Exp. 1-3 and

601   Exp. 1-19, as well as of Exp. 1-12 and Exp. 1-22, indicating that increase in the initial

602   concentration of precursors generally resulted in a minor increment in the absolute signals of

603   HOMs. Clearly, the relative distributions of products in these experiments are quite similar,

604   indicating a minor difference in the relative distributions of products caused by fluctuations of

605   initial concentrations of TMB.

606   3.2.1 HOM monomers

607   Previous studies indicate that oxidation products derived from the peroxide-bicyclic

608   pathway represent a main fraction of HOMs (Wang et al., 2017; Zaytsev et al., 2019). For 1,3,5-

609   TMB, this pathway, as recommended by MCM, starts from a BPR, $C_9H_{13}O_5\cdot$ (MCM name:

610   TM135BPRO2) (Molteni et al., 2018). According to MCM and Molteni et al. (2018), Scheme

611   1 has been proposed to provide a good understanding of this reaction system and the structures

612   of oxidation products. Molteni et al. (2018) suggested that $C_9H_{13}O_7\cdot$, i.e., peroxy radical formed

613   from autooxidation of $C_9H_{13}O_5\cdot$ has two isomers. A second-step of endo-cyclization is required

614   in the formation of one of the isomer, which is extremely slow and not competitive as shown

615   in several previous studies using both experimental and theoretical approaches (Wang et al.,

616   2017; Xu et al., 2020). Even if such a second O_2 bridging to a double bond is assumed to be

617   possible, the abundance of this isomer should be significantly smaller than the other one,

618   because of the much faster reaction rate of H-shift reaction. Therefore, we do not take the

619    $C_9H_{13}O_7\cdot$ isomer containing a double endo-cyclization into consideration in this work. The

620   majority of HOM monomers is generated from subsequent reactions of $C_9H_{13}O_5\cdot$ and newly

621   formed $C_9H_{13}O_7\cdot$, both of which contain one C=C bond in the carbon backbone and thus have

622   a feasible site for OH addition. Meanwhile, the autoxidation reaction rate for newly formed

623    $C_9H_{13}O_7\cdot$ should be significantly smaller than $C_9H_{13}O_5\cdot$, as there is no hydrogen atom in

624 $C_9H_{13}O_7\cdot$ that is able to undergo a hydrogen atom shift at an appreciable rate based on our
625 current understanding. Therefore, the subsequent autoxidation reaction should not be able to
626 generate large amounts of more oxidized RO_2.

627   Monomeric termination products of BPR, as shown in Scheme 1, were not detected by
628 nitrate CIMS in this round of experiments, which might be due to the fast sub-sequential OH
629 oxidation of these products under high [OH] environment since they were observed under low
630 [OH] environments as shown in Section 3.3. Monomeric termination products of $C_9H_{13}O_7\cdot$ were
631 all observed clearly, including $C_9H_{12}O_6$, $C_9H_{14}O_6$, and $C_9H_{14}O_7$. Especially, $C_9H_{14}O_7$ was the
632 most abundant one among all of the HOM monomer products (Figure 2a). As proved by a
633 previous study, these three species should be typical first-generation stabilized products derived
634 from autoxidation (Wang et al., 2020b). These HOM monomers should consist of several
635 isomers bearing the same formula, because products from the secondary reactions cannot share
636 the same structure as that of the one from the first-generation reaction. However, limited by the
637 inherent disadvantages of mass spectrometers, we could not distinguish isomers here and
638 further illustrate their different chemical behaviors.

639
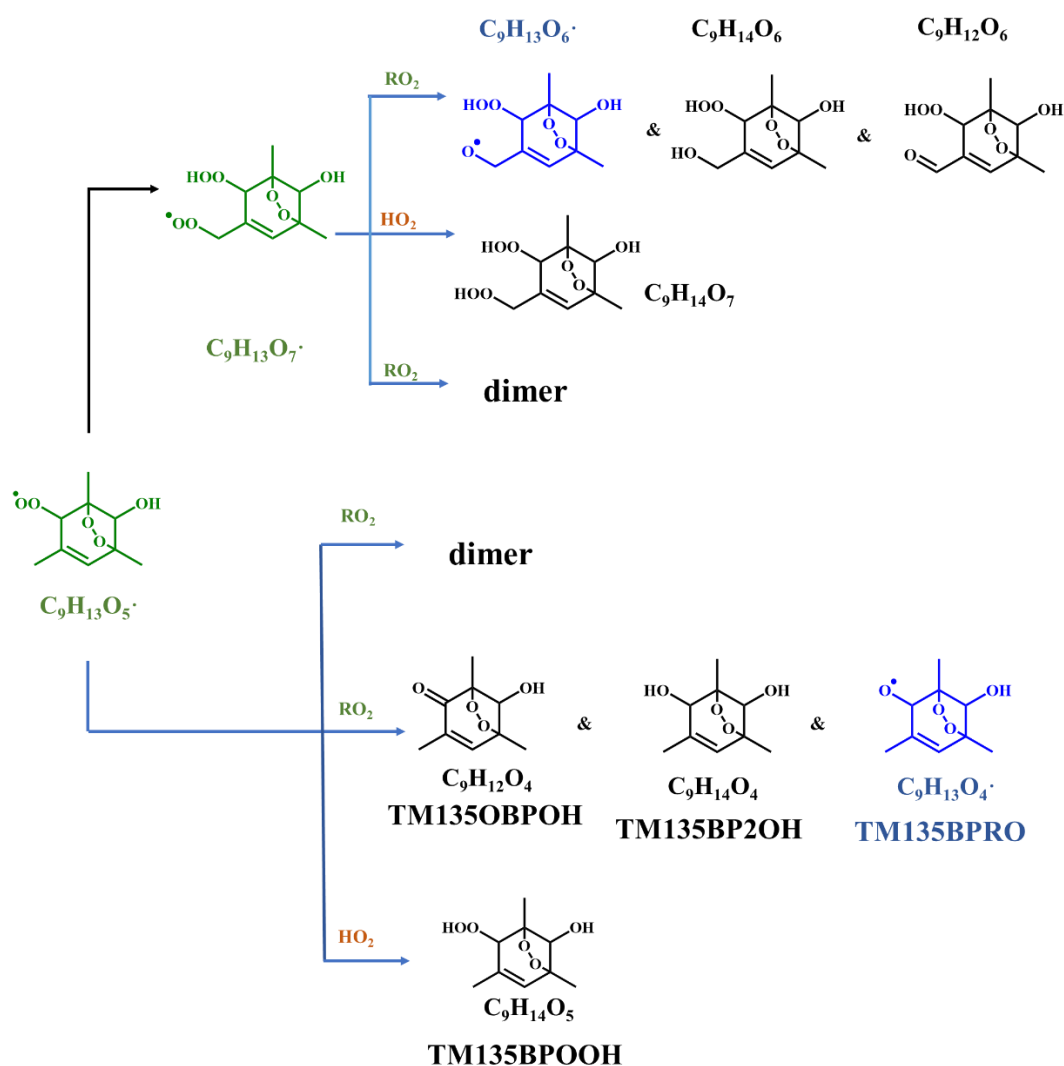
Scheme 1. Oxidation pathways of the bicyclic peroxy radical $C_9H_{13}O_5 \cdot$ (MCM name: TM135BPRO2) in the OH-initiated oxidation of 1,3,5-TMB. Green, blue, and black formulae denote alkyl peroxy radicals, alkoxy radicals and stabilized products, respectively. Black arrows denote the autoxidation pathway. MCM names for HO_2- and RO_2-termination products of TM135BPRO2 are present.

In addition to these three ones, the next most prominent products to $C_9H_{14}O_7$ were $C_9H_{16}O_7$ and $C_9H_{16}O_8$ (Figure 3a), which are produced from multi-generation oxidation according to their DBE. Based on the formulae of these three HOM monomers, they ($C_9H_{14}O_7$, $C_9H_{16}O_7$, and $C_9H_{16}O_8$) could be formed from the bimolecular termination reactions of $C_9H_{15}O_8 \cdot$, which can be generated by an OH attack to $C_9H_{14}O_5$ (Scheme 2), the hydroperoxyl termination product of the BPR, $C_9H_{13}O_5 \cdot$. The other HOM monomers characterized with high signals were $C_9H_{14}O_8$ and $C_9H_{16}O_9$ (Figure 3b). These two HOM monomers ($C_9H_{14}O_8$ and $C_9H_{16}O_9$), together with $C_9H_{16}O_8$, correspond to the monomeric termination products of $C_9H_{15}O_9 \cdot$, which is highly likely

23

653   the peroxy radical generated by an OH attack to $C_9H_{14}O_6$ (Scheme 3), i.e., the hydroxyl

654   termination product of $C_9H_{13}O_7\cdot$. As discussed earlier, $C_9H_{13}O_7\cdot$ is a typical autoxidation

655   reaction product of the BPR of $C_9H_{13}O_5\cdot$. Therefore, detected signals of $C_9H_{16}O_8$ should be the

656   sum of two isomers' signals at least. Other HOM monomers were generally observed at much

657   lower signals and thus were not plotted individually.

658   **(a)**

659

660   **(b)**

661
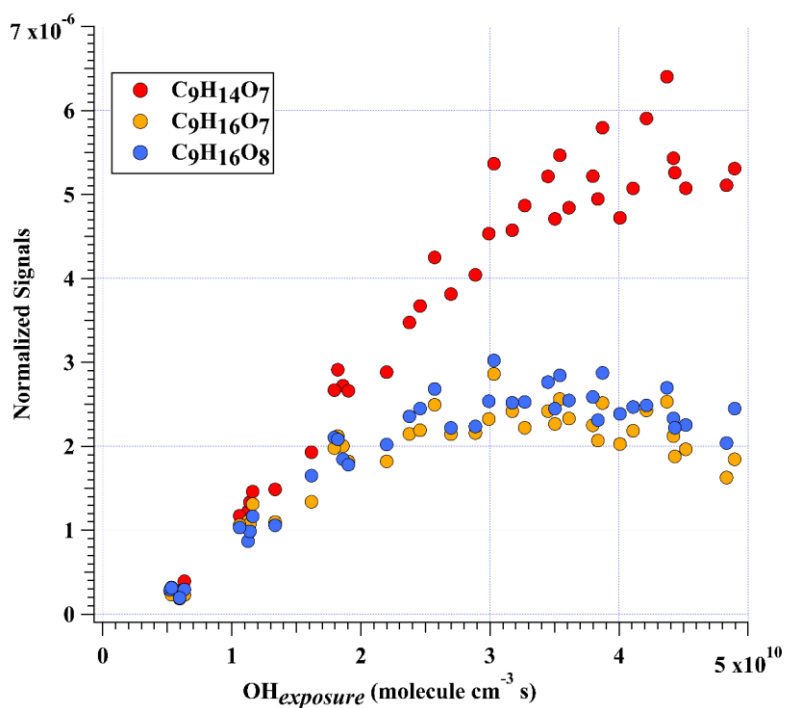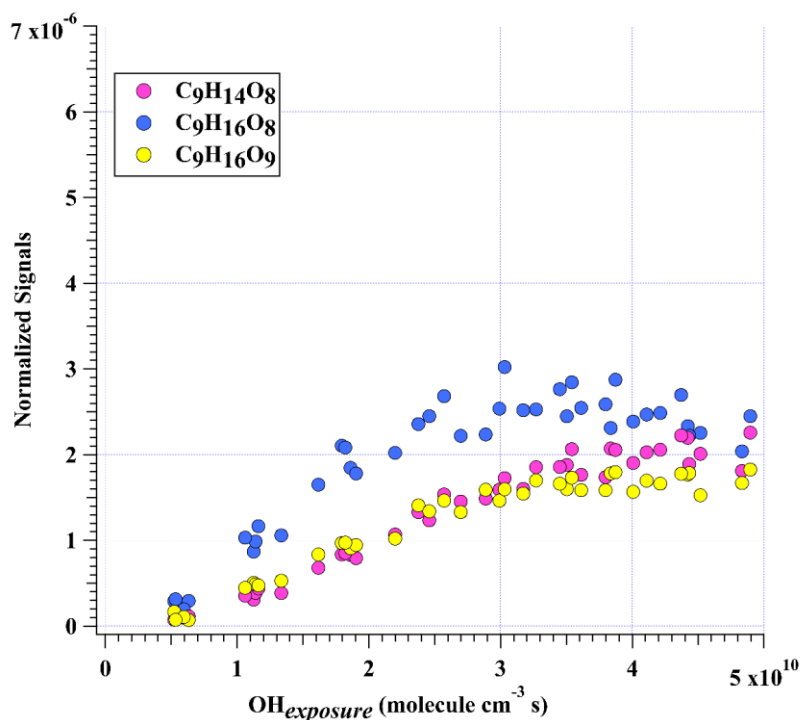
Figure 3. Normalized signals of (a) $C_9H_{14}O_7$, $C_9H_{16}O_7$, and $C_9H_{16}O_8$ and (b) $C_9H_{14}O_8$, $C_9H_{16}O_8$, and $C_9H_{16}O_9$ measured at the exit of OFR in our high [OH] experiments without NO_x as a function of OH exposure. $C_9H_{16}O_8$ are shown in both plots to better illustrate the chemical profiles of different compound groups.

666
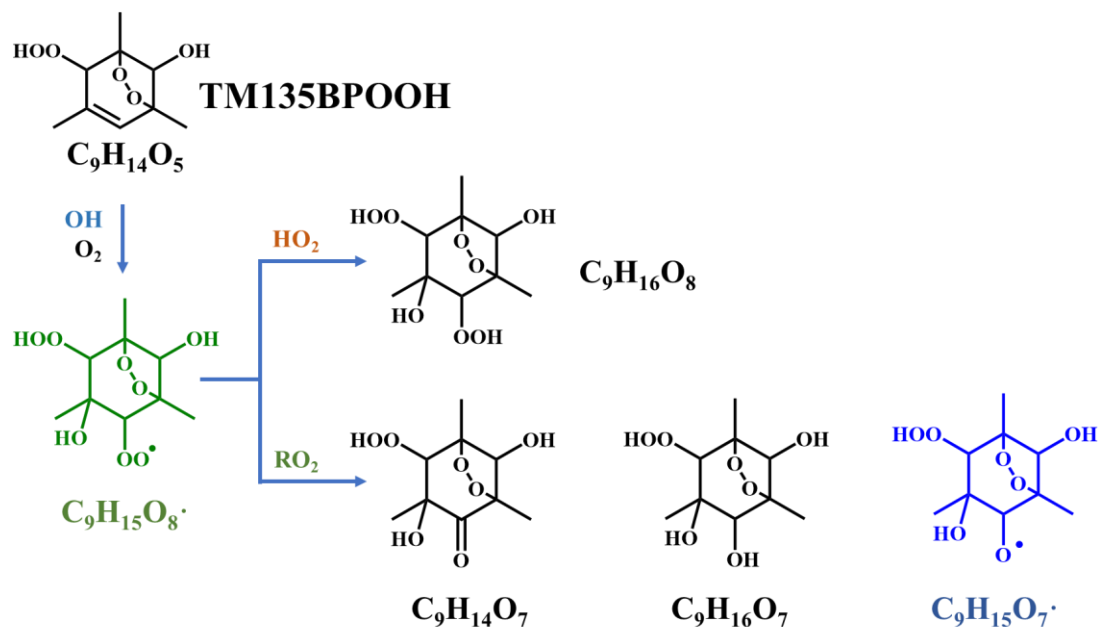
Scheme 2. Proposed formation pathways of $C_9H_{14}O_7$, $C_9H_{16}O_7$, and $C_9H_{16}O_8$ via the secondary OH oxidation of TM135BPOOH.

25
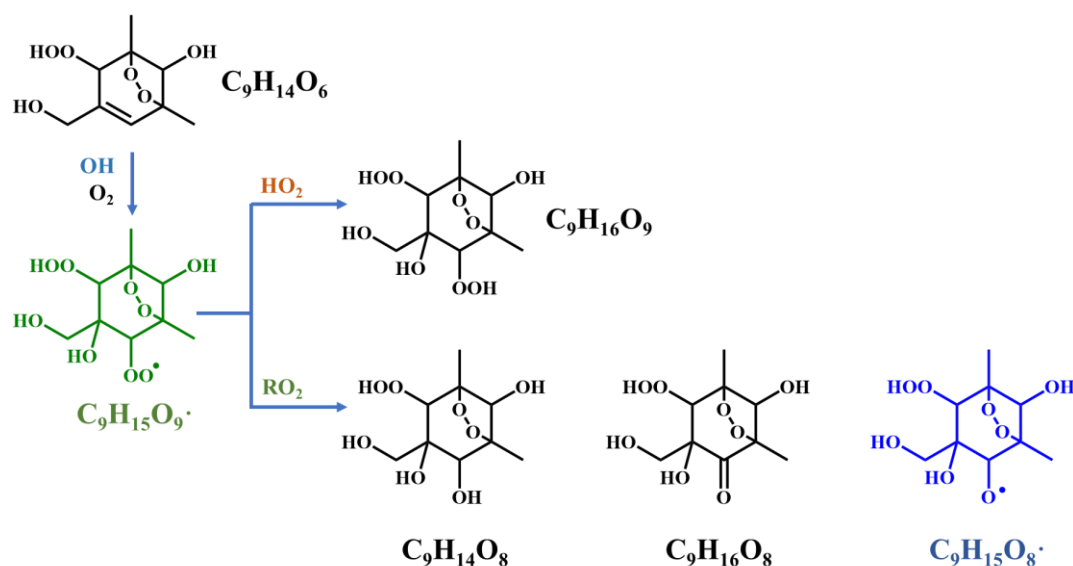
Scheme 3. Proposed formation pathways of $C_9H_{14}O_8$, $C_9H_{16}O_8$, and $C_9H_{16}O_9$ via the secondary OH oxidation of TM135BPOOH.

It is worth noting that HOM monomers with 18 hydrogen atoms, i.e., a DBE of 1, were never observed in our experiments, including a potential stabilized hydroperoxyl products formed from $C_9H_{17}O_m\cdot$. This is expected, since $C_9H_{17}O_m\cdot$ should be in really low concentrations, if ever existed. As indicated by its hydrogen number, a $C_9H_{17}O_m\cdot$ was formed by at least two OH additions to the C=C bond of a $C_9H_{13}O_m\cdot$, but the main BPR, $C_9H_{13}O_5\cdot$, and its autoxidation product ($C_9H_{13}O_7\cdot$), are characterized with one C=C bond on the ring, which makes this formation pathway impossible. Other ring-breakage pathways should not contribute to the formation of this radical ($C_9H_{17}O_m\cdot$) because of their low branching ratio as determined by recent studies (Zaytsev et al., 2019; Xu et al., 2020).

Proposed according to MCM and Molteni et al. (2018), scheme 4 shows the NO termination pathways of the main BPR $C_9H_{13}O_5\cdot$ and its autoxidation product, $C_9H_{13}O_7\cdot$. After introducing N_2O into PAM OFR, quantities of organonitrates were generated, including both C9 and C18 organonitrates. The averaged mass spectrometry of nitrate CIMS in the 4.41×10^{10} molecule cm^{-3} NO experiment and 1.18×10^{11} molecule cm^{-3} NO experiment is shown in Figure S3. Organonitrates were formed via the NO + RO_2 reaction, called as NO termination reactions. The distribution of oxidation products under these two NO settings were similar.
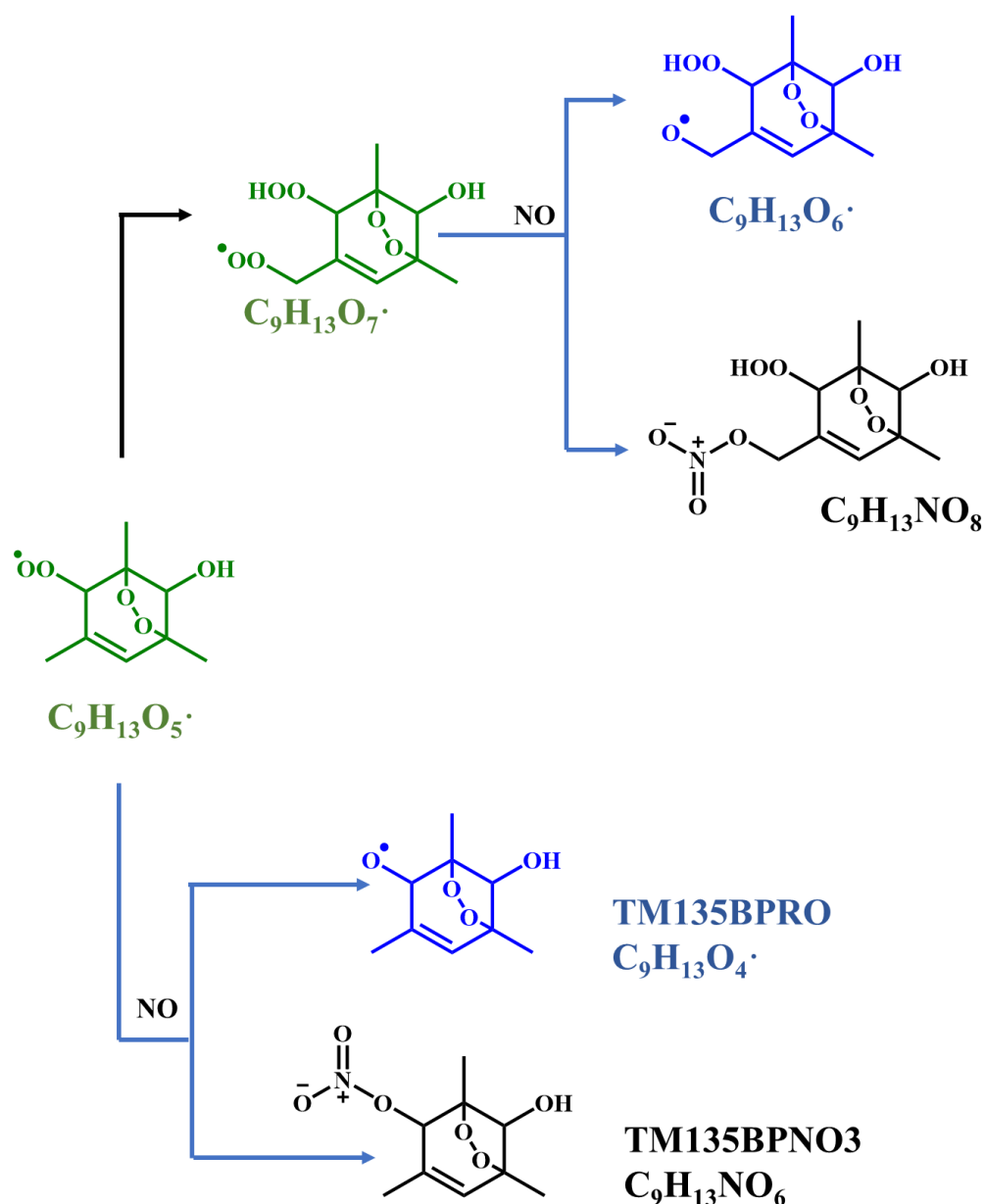
Scheme 4. NO termination reactions of the bicyclic peroxy radical $C_9H_{13}O_5\cdot$ (MCM name: TM135BPRO2) and its autoxidation reaction products. Green, blue, and black formulae denote alkyl peroxy radicals, alkoxy radicals and stabilized products, respectively. Black arrows denote the autoxidation pathway. MCM names of NO-termination products of TM135BPRO2 are present.

As discussed above, most of the first-generation HOMs should contain a C=C bond in the carbon backbone. The ubiquitous existence of organonitrates that contain two nitrogen atoms exactly confirms the extensive secondary OH oxidation in the systems, because the NO termination reaction of RO_2 is the only pathway that can generate organonitrates in our experiments and this pathway can only introduce one nitrogen atom at a time, as indicated in Scheme 4. RO_2 can react with NO_2 to form peroxynitrates ($ROONO_2$) but these species are

700 thermally unstable except at very low temperatures or when the RO_2 is an acylperoxy radical

701 (Orlando and Tyndall, 2012), neither of which were not met in our experiments. The

702 concentrations of NO_3 were estimated to be lower than 2.45×10^7 molecule cm^{-3} by our modified

703 PAM_chem_v8 because of the existence of decent concentrations of NO, which would

704 consume NO_3 at a rapid reaction rate, i.e., 2.7×10^{-11} molecule^{-1} cm^3 s^{-1} (IUPAC dataset ,

705 https://iupac-aeris.ipsl.fr, last access: 26 October 2023). Therefore, NO_2 and NO_3 were not

706 likely to react with RO_2 to form large amounts of organonitrates in our experiments. Taking the

707 most abundant organonitrate, $C_9H_{14}N_2O_{10}$, as an example, it was exactly the NO termination

708 product of $C_9H_{14}NO_9\cdot$, which was generated from an OH attack and a subsequent O_2 addition

709 to $C_9H_{13}NO_6$, the NO termination product of $C_9H_{13}O_5\cdot$. For other organonitrates, $C_9H_{13}NO_8$, the

710 second most abundant organonitrate, could be either a NO termination product of $C_9H_{13}O_7\cdot$ or,

711 together with other most abundant organonitrates, $C_9H_{15}NO_7$ and $C_9H_{15}NO_8$, classical

712 termination products of $C_9H_{14}NO_9\cdot$. $C_9H_{14}N_2O_{10}$, $C_9H_{15}NO_7$, and $C_9H_{15}NO_8$ all have a DBE of

713 2 lower than the precursor and thus are the typical multi-generation OH oxidation products.

714   The NO:RO_2 ratio in the PAM OFR in this series of experiments is lower than typical

715 values in the ambient atmosphere, which is due to the existence of O_3 that was utilized to

716 generate $O(^1D)$ in the OFR and its rapid reaction rate with NO. However, due to rapid reaction

717 rate constants between NO and RO_2, i.e., around 8.5×10^{-12} molecule^{-1} cm^3 s^{-1}, the reaction rate

718 for the NO termination channel of RO_2 was as fast as around $0.3 - 1.0$ s^{-1}. Large amounts of

719 organonitrates would still be formed, as discussed in Section 3.1. Our conclusion is also valid

720 because of detection of compounds with multiple nitrogen atoms.

721   3.2.2 HOM dimers

722   Accretion reaction $RO_2 + RO'_2 \rightarrow ROOR' + O_2$ is a source of gas-phase dimer

723 compounds from highly oxidized, functional RO_2 radicals (Ehn et al., 2014; Berndt et al., 2018b;

724 Zhao et al., 2018; Berndt et al., 2018a). $C_{18}H_{26}O_8$ and $C_{18}H_{26}O_{10}$ are two typical accretion

725 reaction products in the 1,3,5-TMB + OH system, whose formation pathways have been

726 elucidated (Berndt et al., 2018b). $C_{18}H_{26}O_8$ can only be formed via the accretion reaction of two

727 $C_9H_{13}O_5\cdot$. $C_9H_{13}O_3\cdot$ is not likely to react with $C_9H_{13}O_7\cdot$ to form large amounts of $C_{18}H_{26}O_8$.

728 $C_9H_{13}O_3\cdot$ can only be formed after addition of a hydroxyl radical to the aromatic ring of 1,3,5-

729 TMB and a subsequent O_2 addition to the newly formed hydroxyl-substituted cyclohexadienyl

730 radical (Vereecken, 2019). However, the lifetime of this radical is extremely short, as $C_9H_{13}O_3\cdot$

731 will undertake a ring-closure reaction and get attached by a O_2 very rapidly, forming BPR,

732 $C_9H_{13}O_5\cdot$. Its short lifetime and low concentration, as indicated by Berndt et al. (2018), lead to

733 its insignificant role in the accretion reactions. In contrast, $C_{18}H_{26}O_{10}$ can be formed either by

734 the accretion reaction between $C_9H_{13}O_5\cdot$ and $C_9H_{13}O_7\cdot$or via a second OH attack to $C_{18}H_{26}O_8$.

735   These two HOM dimers are so far the only ones that are confirmed to be formed via the

736   accretion reactions (Berndt et al., 2018b; Bianchi et al., 2019).

737        $C_{18}H_{26}O_{10}$ was characterized with the highest dimer signals for experiments with OH

738   exposures under 3.5×10^{10} molecule cm^{-3} s. Nevertheless, $C_{18}H_{26}O_{10}$, together with $C_{18}H_{28}O_{12}$,

739     $C_{18}H_{26}O_{12}$, $C_{18}H_{28}O_{11}$, $C_{18}H_{28}O_{13}$, and $C_{18}H_{28}O_{10}$ contributed more than 50% of total HOM

740   dimer signals at any OH exposure levels (Figure 2b). These six most abundant HOM dimers

741   correspond exactly to the hydroperoxyl, hydroxyl, and carbonyl termination products of

742     $C_{18}H_{27}O_{11}\cdot$ and $C_{18}H_{27}O_{13}\cdot$, respectively. These two RO_2 ($C_{18}H_{27}O_{11}\cdot$ and $C_{18}H_{27}O_{13}\cdot$), on the

743   other hand, could be generated by OH attacks to $C_{18}H_{26}O_8$ and $C_{18}H_{26}O_{10}$, respectively, which

744   strongly suggests the significant role of secondary OH chemistry in the formation of HOMs in

745   our experiments. In addition, $C_{18}H_{28}O_x$ can also be formed through accretion of a $C_9H_{13}O_m\cdot$

746   radical and a $C_9H_{15}O_m\cdot$ radical, as suggested by previous studies (Molteni et al., 2018;

747   Tsiligiannis et al., 2019). However, since a $C_9H_{15}O_m\cdot$ radical, as suggested by its hydrogen atom

748   number, can only be formed via an OH addition to the stabilized $C_9H_{14}O_m$ products through

749   multi-generation OH reactions, our conclusion that $C_{18}H_{28}O_x$ are multi-generation OH

750   oxidation products still holds. Figure 4 shows the normalized signals of these abundant HOM

751   dimers at different OH exposures.

752   **(a)**

753
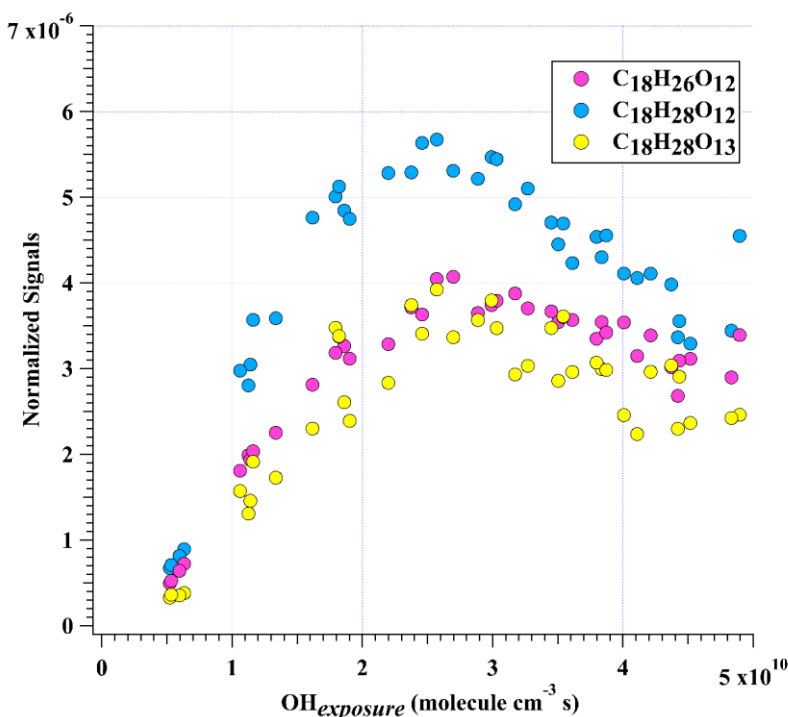
754   **(b)**
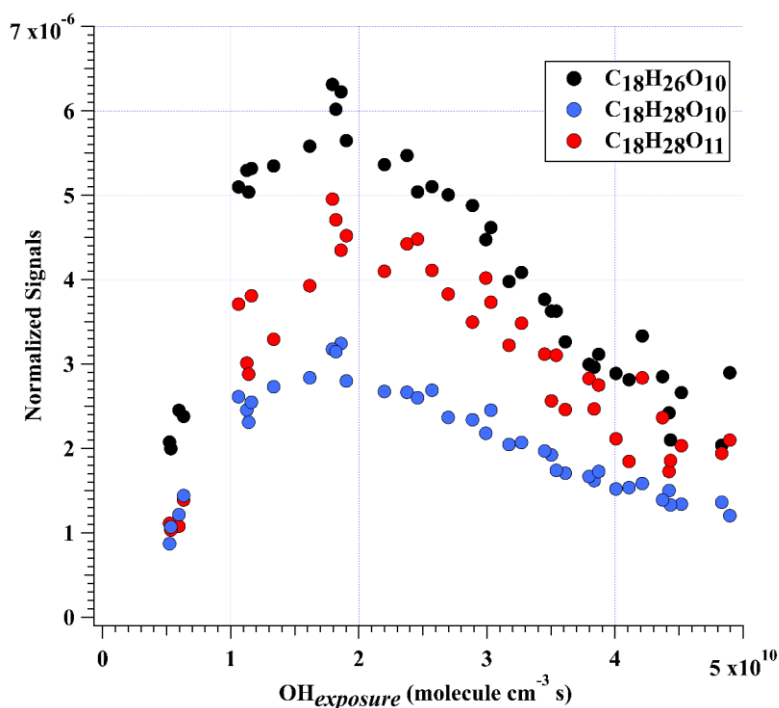
Figure 4. Normalized signals of (a) $C_{18}H_{26}O_{12}$, $C_{18}H_{28}O_{12}$, and $C_{18}H_{28}O_{13}$, and (b) $C_{18}H_{26}O_{10}$, $C_{18}H_{28}O_{10}$, and $C_{18}H_{28}O_{11}$ measured at the exit of OFR in our high [OH] experiments without NO_x as a function of OH exposure.

This decrease of dimer at relatively high OH exposures are likely due to the accelerated accretion reactions in the OFR, resulted by the high RO_2 concentrations. The HOM dimers are formed earlier compared to under ambient conditions and then can go through the further oxidation reactions. Note that this does not mean the maximum concentrations of HOM dimers will also accurately occur at the same OH exposures in the atmosphere, because the detailed appearance time of the maximum concentrations of HOM dimers is dependent on their formation rate and loss rate. In our experiments, the formation rate and loss rate were not accelerated equally. On the other hand, the loss pathways of HOM dimers were not exactly the same as the ambient. This series of experiments are not meant to specifically find out the detailed OH exposures when the maximum concentrations of HOM dimers will occur, but try to indicate how HOM dimers evolve with the increase of OH exposures. This work can be regarded as an indicator for the potential chemical fates of HOM dimers in the atmosphere if their survival time permitted. It should be noted that the gas-phase chemistry in the PAM OFR cannot be exactly the same as that in the ambient. Reactions of OH with OVOCs often lead to HO_2 formation, resulting in a HO_2:RO_2 ratio larger than 1 in the real atmosphere (Bianchi et al., 2019). A recent campaign conducted at a rural site in the Yangtze River Delta estimated that the local ratio of HO_2:RO_2, the latter of which was presumably derived from longer chain alkanes (> C_3), alkenes, and aromatic compounds, was around 1.66 (Ma et al., 2022). Such a

777   high HO_2:RO_2 ratio condition is typically difficult to be simulated in the laboratory experiments,

778   as the precursors are usually hydrocarbons without any OVOCs (Peng and Jimenez, 2020). This

779   is exactly the case for our experiments, but its influences on our conclusion were tiny, as have

780   been discussed in the Section 3.1. Therefore, the difference in the distribution of products will

781   not change our conclusion.

782   Such an active secondary OH chemistry is consistent with the fast OH reaction rates of

783   HOMs. We take $C_{18}H_{26}O_8$ whose plausible structure is shown in Figure S4 as an example,

784   which is the accretion product of two $C_9H_{13}O_5\cdot$. Its OH reaction rate constant is estimated to be

785   around 2.07×10^{-10} cm^3 $molecule^{-1}$ s^{-1} according to the structure-activity relationship (Jenkin et

786   al., 2018b, a), whose details are provided in Supplementary Text S1. This rate is several times

787   larger than that of 1,3,5-TMB, which enables a very active secondary OH chemistry in the

788   system. MCM recommended an OH reaction rate of 1.28×10^{-10} cm^3 $molecule^{-1}$ s^{-1} for

789   TM135BPOOH ($C_9H_{14}O_5$) and 1.00×10^{-10} cm^3 $molecule^{-1}$ s^{-1} for TM135OBPOH ($C_9H_{12}O_4$)

790   (Jenkin et al., 2003). The OH reaction rate for $C_{18}H_{26}O_8$ should also be fast due to the C=C

791   bonds in its structure, which is activated by the adjacent functionalities. Our calculation result

792   is consistent with this estimation.

793   The distributions of C18 organonitrates also verified the extensive secondary reactions.

794   The most abundant C18 organonitrate, $C_{18}H_{27}NO_{12}$ was a NO termination product of radical

795   $C_{18}H_{27}O_{11}\cdot$, which, as mentioned above, was the radical generated from the OH reaction with

796   $C_{18}H_{26}O_8$. $C_{18}H_{27}NO_{12}$ can also be formed either by accretion between a $C_9H_{15}O_m\cdot$ radical and

797   a $C_9H_{12}NO_m\cdot$ radical or accretion between a $C_9H_{13}O_m\cdot$ radical and a $C_9H_{14}NO_m\cdot$ radical. Both

798   $C_9H_{15}O_m\cdot$ and $C_9H_{14}NO_m\cdot$ radicals are a typical multi-generation RO_2 and thus prove

799   $C_{18}H_{27}NO_{12}$ is a multi-generation OH oxidation product. Other C18 organonitrates are believed

800   to be formed in a similar pathway. Hence, plenty of organonitrates have been formed via the

801   multi-generation OH reactions of first-generation stabilized products.

802   **3.3 Oxidation products in low [OH] experiments**

803   Given the larger sampling port, lower initial ozone concentrations, lower UV light

804   intensities, and a better performance of mass spectrometer in this series of low [OH]

805   experiments, a number of new species were detected in the 2nd-round experiments, including

806   three typical termination reaction products of BPR, i.e., $C_9H_{14}O_4$, $C_9H_{14}O_5$, and $C_9H_{13}NO_6$, and

807   a number of low volatile compounds, e.g., $C_9H_xO_{11}$ ($x = 12 - 15$). The distributions of oxidation

808   products detected by nitrate CI-TOF in Exp. 2-3, 2-4, and 2-7, representative low [OH]

809   experiments, are displayed in Figure 5. The detailed molecular formula and their contributions

810   to total HOMs signals are provided in Tables S6 and S7.

811   In addition, certain C9 and C18 HOMs with lower DBE than typical first-generation

812   products predicted by MCM (Saunders et al., 2003) or reported by previous studies (Berndt et

813   al., 2018b), were detected in Exp. 2-3, 2-4, and 2-7, although [OH] in these experiments are

814   much lower than those in the 1st-round experiments.

815   Observation of compounds with lower DBE in Exp. 2-3, 2-4, and 2-7 including HOM

816   monomers with DBE lower than 3 and HOM dimers with DBE lower than 6, as well as

817   monomer radicals with DBE lower than 3 including $C_9H_{15}O_m\cdot$ ($m = 7 - 11$) and $C_9H_{14}NO_9\cdot$,

818   proves the re-initiation of OH oxidation of the stabilized products in experiments with

819   atmospheric relevant [OH]. All the stabilized products and radicals depicted in the proposed

820   mechanisms (Scheme 2 and Scheme 3) were detected in both Exp. 2-3 and Exp. 2-4, except for

821    $C_9H_{15}O_9\cdot$ that was only detected in Exp. 2-3. This means that the proposed reaction pathways

822   have already happened under atmospheric [OH] conditions with limited OH exposures.

823   However, as we do not know the exact structures of these OOMs and radicals, the proposed

824   reaction pathways are merely based on the chemical formulae detected by nitrate CIMS and

825   nitrate CI-TOF and proposed according to the general mechanisms of OH addition reactions to

826   the C=C bond. Other reaction pathways to generate these compounds or other isomers

827   generated in these pathways are undoubtedly feasible.

828   A lot of compounds detected in the experiments without NO_x were not observed in the

829   counterpart experiments with NO_x. We also did not detect decent signals of HOM dimers in the

830   NO_x-present experiments in the 2nd-round experiments. Such a dramatic decrease in the

831   abundance of HOM dimers after the introduction of NO_x into the aromatic oxidation system

832   has been reported in several previous studies (Garmash et al., 2020; Wang et al., 2020b;

833   Tsiligiannis et al., 2019). This might come from the dominant significance of NO + RO_2

834   reactions ($R8 - R9$) after the introduction of NO_x into system, making signals of certain HOMs

835   from other channels lower than the detection limit of the instrument. The proportions of other

836   reaction channels decreased, and were reassigned to the NO channel, as evidenced by the fact

837   that most of observed oxidation products were organonitrates, which is in an excellent

838   agreement with the modeled channel proportions in Section 3.1.

839   Many organonitrates were observed in both series of experiments. In the low [OH]

840   experiments, the most significant compound was $C_9H_{13}NO_8$, whose formula matches the NO

841   termination product of $C_9H_{13}O_7\cdot$, i.e., autoxidation product of BPR. The second most important

842   compound, $C_9H_{14}N_2O_{10}$ in our low [OH] experiments, was the most significant product in the

843   high [OH] experiments in presence of NO_x, whose formula matches the NO termination product

844   of $C_9H_{14}NO_9\cdot$, i.e., the RO_2 formed via an OH addition to $C_9H_{13}NO_6$, the NO termination

845   product of BPR. All of the products and radicals mentioned above were observed in Exp. 2-7,

846   as shown in Figure 5c. From the perspective of molecular formula, $C_9H_{14}N_2O_{10}$ is also one of

847   the most frequently observed multi-nitrogen-containing compound in polluted atmospheres,

848   whose seasonal variations show a good correlation with [OH] (Guo et al., 2022; Yang et al.,

849   2023).

850   A comparison of relative abundances of C9 and C18 products under different [OH] levels

851   is helpful for the elucidation of their formation pathways. The difference in product

852   distributions between Exp. 2-3 ([OH] = ~1.69×10^7 molecule cm^{-3}) and Exp. 2-1 ([OH] =

853   ~1.03×10^8 molecule cm^{-3}), as well as between Exp. 2-3 and Exp. 1-12 ([OH] = ~8.47×10^8

854   molecule cm^{-3}) is shown in Figure 6. The normalized abundance was obtained by normalizing

855   all the products to the most abundant one in each experiment, i.e., $C_{18}H_{26}O_{10}$ in Exp. 2-1 and

856   Exp. 2-3, and $C_9H_{14}O_7$ in Exp. 1-12. The changes in the normalized abundance were obtained

857   by subtracting the normalized abundance in Exp. 2-1 from that in Exp. 2-3, and Exp. 1-12 from

858   Exp. 2-3. As the [OH] and OH exposure increased, there was a noticeable rise in the relative

859   abundance of more oxygenated compounds, which can be attributed to the larger proportion of

860   multi-generation OH oxidation in high OH exposure experiments. This comparison

861   demonstrates the capacity and potential of multi-generation OH oxidation to reduce DBE and

862   elevate the oxygenated levels of oxidation products.

863   In conclusion, observation of the same low DBE compounds, i.e., DBE = 2, in both low

864   [OH] and high [OH] experiments confirms the feasibility of the generation of HOMs under

865   atmospheric relevant conditions. The detection of $C_9H_{14}O_5$, $C_9H_{15}O_8\cdot$, $C_9H_{14}O_7$, $C_9H_{14}O_8$,

866    $C_9H_{15}O_7\cdot$, and $C_9H_{16}O_8$, and $C_9H_{14}O_6$, $C_9H_{15}O_9\cdot$, $C_9H_{14}O_8$, $C_9H_{14}O_9$, $C_9H_{15}O_8\cdot$, and $C_9H_{16}O_9$, in

867   low [OH] experiments also confirms the potential existence of the proposed mechanisms, i.e.,

868   Scheme 2 and Scheme 3, respectively. Certainly, other potential formation pathways for these
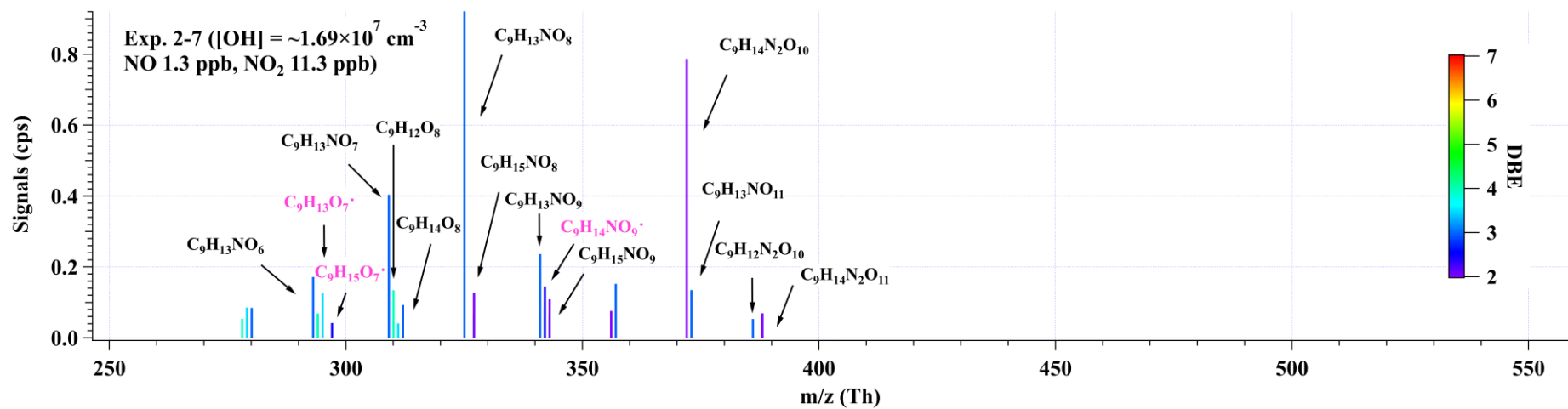
869   products are possible.

(a)
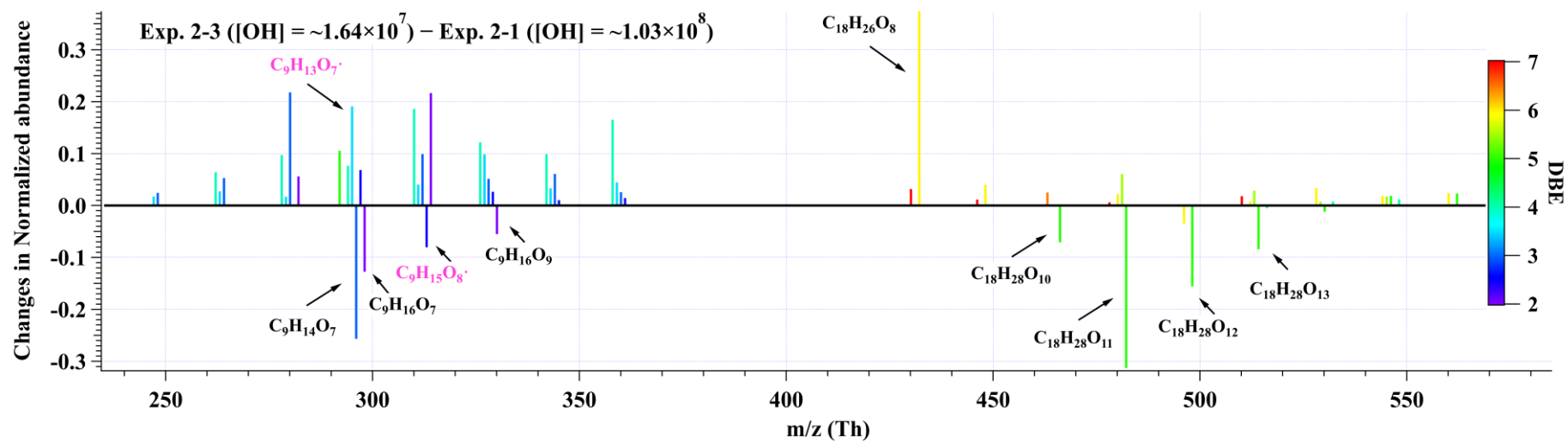
(b)
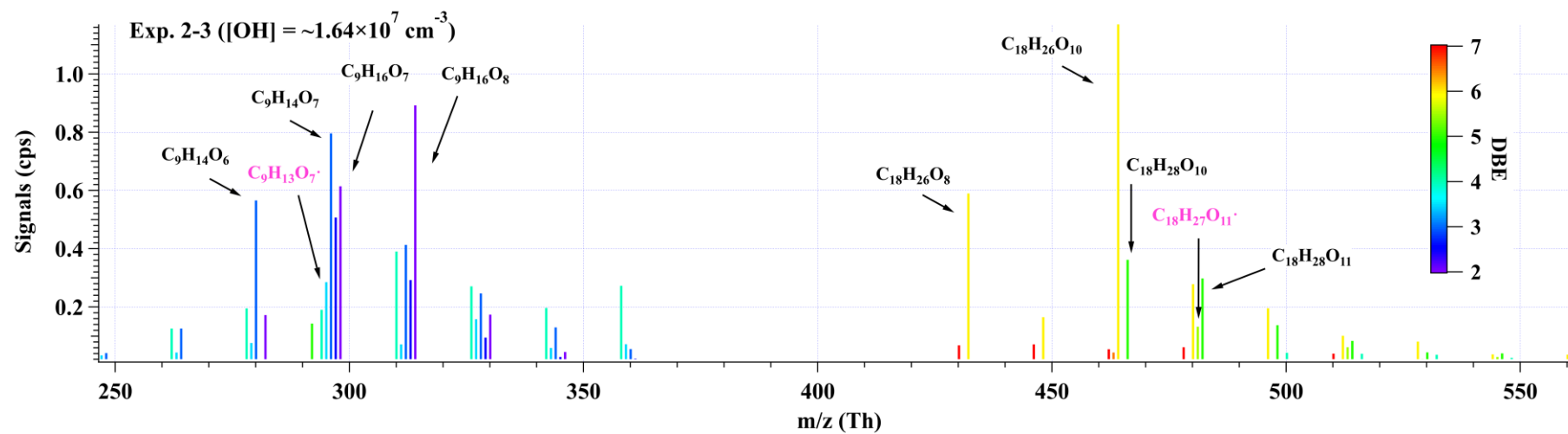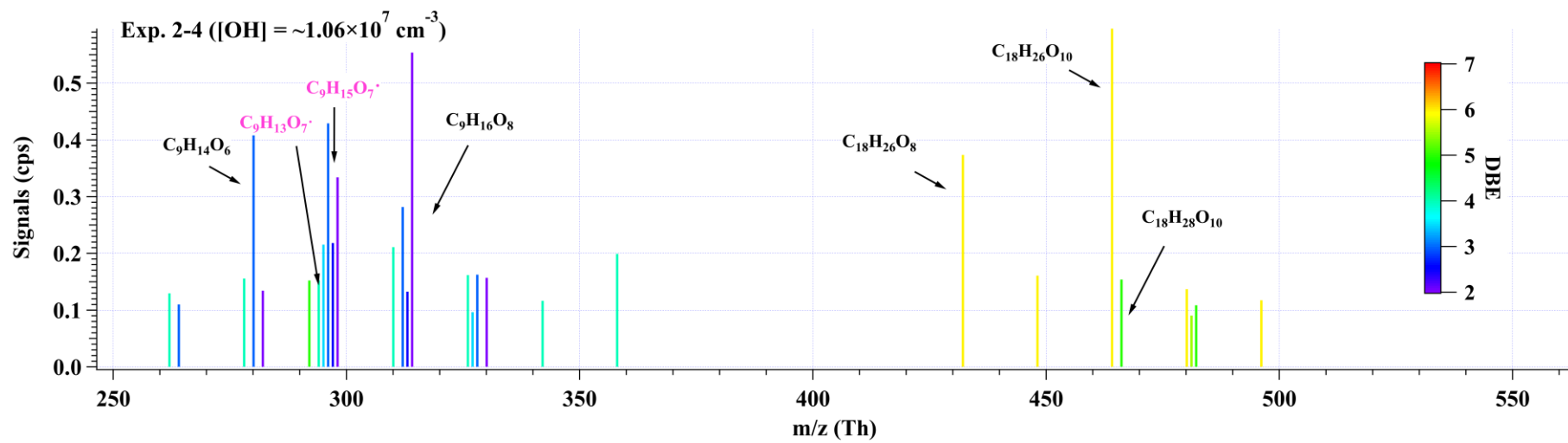
874　**(c)**

875
876

877　**Figure 5.** Distributions of C9 and C18 products detected by nitrate CI-TOF in (a) Exp. 2-3, (b) Exp. 2-4, and (c) Exp. 2-7. The reagent ion, NO_3^-, is omitted in
878　the label for the molecular formula. Important radicals were labelled in pink. Note that no convinced signals of HOM dimers were observed in the 2nd-round
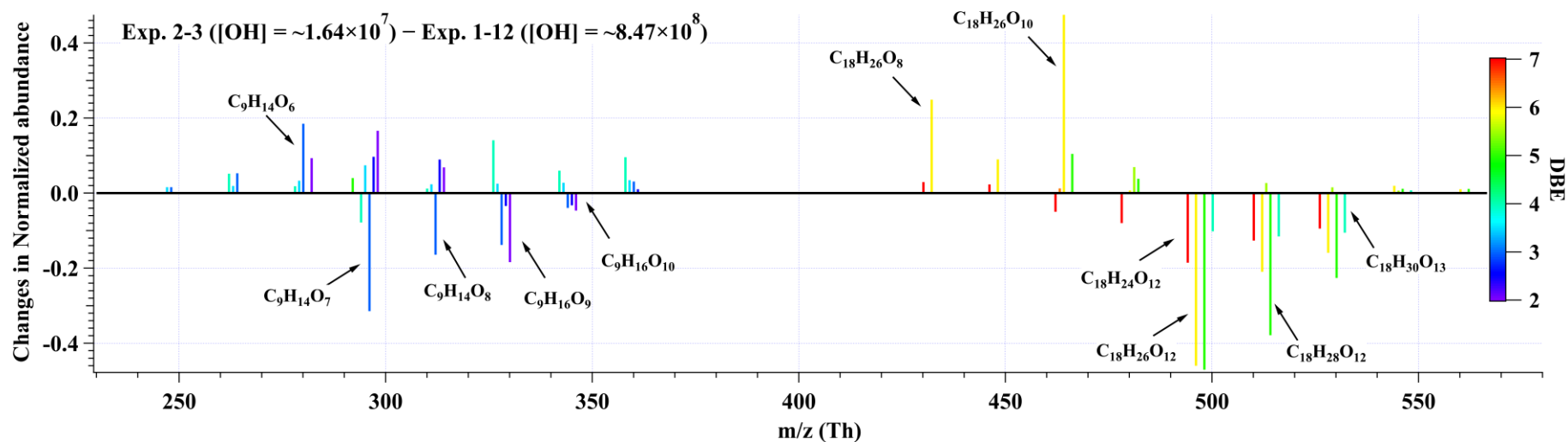879　experiments with NO_x.

880

881

(a)

883

(b)

37

885

886 **Figure 6**. The changes in normalized abundance of C9 and C18 products observed by nitrate CI-TOF in (a) Exp.2-3 relative to Exp.2-1, and (b) Exp.2-3 relative

887 to Exp.1-12. The reagent ion, NO_3^-, is omitted in the label. The normalized abundance was obtained by normalizing all the products to the most abundant one

888 in each experiment, i.e., $C_{18}H_{26}O_{10}$ in Exp.2-1 and Exp.2-3, and $C_9H_{14}O_7$ in Exp.1-12.

4 Atmospheric Implications

This study highlights the influences of OH exposure on the distribution and evolution of 1,3,5-TMB-derived HOMs. Secondary OH reactions can influence HOMs' composition by directly reacting with the stabilized first-generation oxidation products, leading to enhanced formation of HOMs, if the stabilized, first-generation oxidation products could survive from condensation loss onto pre-existing particles. Observation of organonitrates generated in the NO experiments further confirmed the secondary OH oxidation. Due to the elevated abundance and the reduced volatility of HOMs, growth rates of newly formed nanoparticles in the presence of HOMs could be raised, especially in high-OH environments, which prevails in the summer noon. Substantially high concentrations of OH have been frequently observed in polluted environments during summer, e.g., megacities in China (Tan et al., 2019), and thus more active secondary OH reactions are expected compared to wintertime. As a plausible consequence, seasonal differences of HOMs and new particle formation (NPF) are resulted (Qiao et al., 2021; Yao et al., 2018; Guo et al., 2022). Furthermore, previous studies suggest that high concentrations of NO can suppress the formation of HOMs via the suppression of autoxidation (Pye et al., 2019), but the influences of such a suppression could have been overestimated, since secondary OH reactions can continue to oxidize the stabilized organonitrates. Our conclusions help to explain the existing gap between model prediction and ambient measurement on the HOMs concentrations (Qi et al., 2018), and to build a global HOMs simulation model.

References

Assaf, E., Song, B., Tomas, A., Schoemaecker, C., and Fittschen, C.: Rate Constant of the Reaction between CH 3 O 2 Radicals and OH Radicals Revisited , J. Phys. Chem. A, 120, 8923–8932, https://doi.org/10.1021/acs.jpca.6b07704, 2016.

Assaf, E., Tanaka, S., Kajii, Y., Schoemaecker, C., and Fittschen, C.: Rate constants of the reaction of C2–C4 peroxy radicals with OH radicals, Chem. Phys. Lett., 684, 245–249, https://doi.org/10.1016/j.cplett.2017.06.062, 2017.

Berndt, T., Mentler, B., Scholz, W., Fischer, L., Herrmann, H., Kulmala, M., and Hansel, A.: Accretion Product Formation from Ozonolysis and OH Radical Reaction of α-Pinene: Mechanistic Insight and the Influence of Isoprene and Ethylene, Environ. Sci. Technol., 52, 11069–11077, https://doi.org/10.1021/acs.est.8b02210, 2018a.

Berndt, T., Scholz, W., Mentler, B., Fischer, L., Herrmann, H., Kulmala, M., and Hansel, A.: Accretion Product Formation from Self- and Cross-Reactions of RO2 Radicals in the Atmosphere, Angew. Chemie - Int. Ed., 57, 3820–3824, https://doi.org/10.1002/anie.201710989, 2018b.

Bianchi, F., Kurtén, T., Riva, M., Mohr, C., Rissanen, M. P., Roldin, P., Berndt, T., Crounse, J. D., Wennberg, P. O., Mentel, T. F., Wildt, J., Junninen, H., Jokinen, T., Kulmala, M., Worsnop, D. R., Thornton, J. A., Donahue, N., Kjaergaard, H. G., and Ehn, M.: Highly Oxygenated Organic Molecules (HOM) from Gas-Phase Autoxidation Involving Peroxy Radicals: A Key Contributor to Atmospheric Aerosol, Chem. Rev., 119, 3472–3509, https://doi.org/10.1021/acs.chemrev.8b00395, 2019.

Bossolasco, A., Faragó, E. P., Schoemaecker, C., and Fittschen, C.: Rate constant of the reaction between CH3O2 and OH radicals, Chem. Phys. Lett., 593, 7–13, https://doi.org/10.1016/j.cplett.2013.12.052, 2014.

Brune, W. H.: The Chamber Wall Index for Gas-Wall Interactions in Atmospheric Environmental Enclosures, Environ. Sci. Technol., 53, 3645–3652, https://doi.org/10.1021/acs.est.8b06260, 2019.

Caravan, R. L., Khan, M. A. H., Zádor, J., Sheps, L., Antonov, I. O., Rotavera, B., Ramasesha, K., Au, K., Chen, M. W., Rösch, D., Osborn, D. L., Fittschen, C., Schoemaecker, C., Duncianu, M., Grira, A., Dusanter, S., Tomas, A., Percival, C. J., Shallcross, D. E., and Taatjes, C. A.: The reaction of hydroxyl and methylperoxy radicals is not a major source of atmospheric methanol, Nat. Commun., 9, 1–9, https://doi.org/10.1038/s41467-018-06716-x, 2018.

Cheng, X., Chen, Q., Li, Y. J., Zheng, Y., Liao, K., and Huang, G.: Highly Oxygenated Organic Molecules Produced by the Oxidation of Benzene and Toluene in a Wide Range of OH Exposure and NOx Conditions, Atmos. Chem. Phys., 1–23, https://doi.org/10.5194/acp-2021-201, 2021.

Crounse, J. D., Nielsen, L. B., Jørgensen, S., Kjaergaard, H. G., and Wennberg, P. O.: Autoxidation of organic compounds in the atmosphere, J. Phys. Chem. Lett., 4, 3513–3520, https://doi.org/10.1021/jz4019207, 2013.

Deng, C., Fu, Y., Dada, L., Yan, C., Cai, R., Yang, D., Zhou, Y., Yin, R., Lu, Y., Li, X., Qiao, X., Fan, X., Nie, W., Kontkanen, J., Kangasluoma, J., Chu, B., Ding, A., Kerminen, V. M., Paasonen, P., Worsnop, D. R., Bianchi, F., Liu, Y., Zheng, J., Wang, L., Kulmala, M., and

968   Jiang, J.: Seasonal characteristics of new particle formation and growth in urban Beijing,

969   Environ. Sci. Technol., 54, 8547–8557, https://doi.org/10.1021/acs.est.0c00808, 2020.

970   Ehn, M., Thornton, J. A., Kleist, E., Sipilä, M., Junninen, H., Pullinen, I., Springer, M.,

971   Rubach, F., Tillmann, R., Lee, B., Lopez-Hilfiker, F., Andres, S., Acir, I. H., Rissanen, M.,

972   Jokinen, T., Schobesberger, S., Kangasluoma, J., Kontkanen, J., Nieminen, T., Kurtén, T.,

973   Nielsen, L. B., Jørgensen, S., Kjaergaard, H. G., Canagaratna, M., Maso, M. D., Berndt, T.,

974   Petäjä, T., Wahner, A., Kerminen, V. M., Kulmala, M., Worsnop, D. R., Wildt, J., and

975   Mentel, T. F.: A large source of low-volatility secondary organic aerosol, Nature, 506, 476–

976   479, https://doi.org/10.1038/nature13032, 2014.

977   Eisele, F. L. and Tanner, D. J.: Measurement of the gas phase concentration of H_2SO_4 and

978   methane sulfonic acid and estimates of H_2SO_4 production and loss in the atmosphere, J.

979   Geophys. Res. Atmos., 98, 9001–9010, https://doi.org/10.1029/93JD00031, 1993.

980   Fittschen, C.: The reaction of peroxy radicals with OH radicals, Chem. Phys. Lett., 725, 102–

981   108, https://doi.org/10.1016/j.cplett.2019.04.002, 2019.

982   Fuller, E. N., Schettler, P. D., and Giddings, J. C.: A new method for prediction of binary gas-

983   phase diffusion coefficients, Ind. Eng. Chem., 58, 18–27,

984   https://doi.org/10.1021/ie50677a007, 1966.

985   Garmash, O., Rissanen, M. P., Pullinen, I., Schmitt, S., Kausiala, O., Tillmann, R., Zhao, D.,

986   Percival, C., Bannan, T. J., Priestley, M., Hallquist, Å. M., Kleist, E., Kiendler-Scharr, A.,

987   Hallquist, M., Berndt, T., McFiggans, G., Wildt, J., Mentel, T. F., and Ehn, M.: Multi-

988   generation OH oxidation as a source for highly oxygenated organic molecules from

989   aromatics, Atmos. Chem. Phys., 20, 515–537, https://doi.org/10.5194/acp-20-515-2020, 2020.

990   Guo, Y., Yan, C., Liu, Y., Qiao, X., Zheng, F., Zhang, Y., Zhou, Y., Li, C., Fan, X., Lin, Z.,

991   Feng, Z., Zhang, Y., Zheng, P., Tian, L., Nie, W., Wang, Z., Huang, D., Daellenbach, K. R.,

992   Yao, L., Dada, L., Bianchi, F., Jiang, J., Liu, Y., Kerminen, V. M., and Kulmala, M.: Seasonal

993   variation in oxygenated organic molecules in urban Beijing and their contribution to

994   secondary organic aerosol, Atmos. Chem. Phys., 22, 10077–10097,

995   https://doi.org/10.5194/acp-22-10077-2022, 2022.

996   Heinritzi, M., Simon, M., Steiner, G., Wagner, A. C., Kürten, A., Hansel, A., and Curtius, J.:

997   Characterization of the mass-dependent transmission efficiency of a CIMS, Atmos. Meas.

998   Tech., 9, 1449–1460, https://doi.org/10.5194/amt-9-1449-2016, 2016.

999   Hyttinen, N., Kupiainen-Määttä, O., Rissanen, M. P., Muuronen, M., Ehn, M., and Kurtén, T.:

1000   Modeling the Charging of Highly Oxidized Cyclohexene Ozonolysis Products Using Nitrate-

1001   Based Chemical Ionization, J. Phys. Chem. A, 119, 6339–6345,

1002   https://doi.org/10.1021/acs.jpca.5b01818, 2015.

1003   Iyer, S., Kumar, A., Savolainen, A., Barua, S., Daub, C., Pichelstorfer, L., Roldin, P.,

1004   Garmash, O., Seal, P., Kurtén, T., and Rissanen, M.: Molecular rearrangement of bicyclic

1005   peroxy radicals is a key route to aerosol from aromatics, Nat. Commun., 14, 4984,

1006   https://doi.org/10.1038/s41467-023-40675-2, 2023.

1007   Jacob, D. J.: Introduction to atmospheric chemistry, Princeton, 1999.

1008   Jenkin, M. E., Saunders, S. M., Wagner, V., and Pilling, M. J.: Protocol for the development

1009   of the Master Chemical Mechanism, MCM v3 (Part B): tropospheric degradation of aromatic

1010   volatile organic compounds, Atmos. Chem. Phys., 3, 181–193, https://doi.org/10.5194/acp-3-

1011   181-2003, 2003.

1012   Jenkin, M. E., Valorso, R., Aumont, B., Rickard, A. R., and Wallington, T. J.: Estimation of
1013   rate coefficients and branching ratios for gas-phase reactions of OH with aliphatic organic
1014   compounds for use in automated mechanism construction, 9297–9328 pp.,
1015   https://doi.org/10.5194/acp-18-9297-2018, 2018a.
1016   Jenkin, M. E., Valorso, R., Aumont, B., Rickard, A. R., and Wallington, T. J.: Estimation of
1017   rate coefficients and branching ratios for gas-phase reactions of OH with aromatic organic
1018   compounds for use in automated mechanism construction, Atmos. Chem. Phys., 18, 9329–
1019   9349, https://doi.org/10.5194/acp-18-9329-2018, 2018b.
1020   Keller-Rudek, H., Moortgat, G. K., Sander, R., and Sörensen, R.: The MPI-Mainz UV/VIS
1021   spectral atlas of gaseous molecules of atmospheric interest, Earth Syst. Sci. Data, 5, 365–373,
1022   https://doi.org/10.5194/essd-5-365-2013, 2013.
1023   Knap, H. C. and Jørgensen, S.: Rapid Hydrogen Shift Reactions in Acyl Peroxy Radicals, J.
1024   Phys. Chem. A, 121, 1470–1479, https://doi.org/10.1021/acs.jpca.6b12787, 2017.
1025   Krechmer, J., Lopez-Hilfiker, F., Koss, A., Hutterli, M., Stoermer, C., Deming, B., Kimmel,
1026   J., Warneke, C., Holzinger, R., Jayne, J., Worsnop, D., Fuhrer, K., Gonin, M., and De Gouw,
1027   J.: Evaluation of a New Reagent-Ion Source and Focusing Ion− Molecule Reactor for Use in
1028   Proton-Transfer-Reaction Mass Spectrometry, Anal. Chem., 90, 12011–12018,
1029   https://doi.org/10.1021/acs.analchem.8b02641, 2018.
1030   Lambe, A., Massoli, P., Zhang, X., Canagaratna, M., Nowak, J., Daube, C., Yan, C., Nie, W.,
1031   Onasch, T., Jayne, J., Kolb, C., Davidovits, P., Worsnop, D., and Brune, W.: Controlled nitric
1032   oxide production via O(1D) + N2O reactions for use in oxidation flow reactor studies, Atmos.
1033   Meas. Tech., 10, 2283–2298, https://doi.org/10.5194/amt-10-2283-2017, 2017.
1034   Lambe, A., Krechmer, J., Peng, Z., Casar, J., Carrasquillo, A., Raff, J., Jimenez, J., and
1035   Worsnop, D.: HO x and NO x production in oxidation flow reactors via photolysis of, 1–22,
1036   2018.
1037   Lambe, A. T., Ahern, A. T., Williams, L. R., Slowik, J. G., Wong, J. P. S., Abbatt, J. P. D.,
1038   Brune, W. H., Ng, N. L., Wright, J. P., Croasdale, D. R., Worsnop, D. R., Davidovits, P., and
1039   Onasch, T. B.: Characterization of aerosol photooxidation flow reactors: heterogeneous
1040   oxidation, secondary organic aerosol formation and cloud condensation nuclei activity
1041   measurements, Atmos. Meas. Tech, 4, 445–461, https://doi.org/10.5194/amt-4-445-2011,
1042   2011.
1043   Lambe, A. T., Chhabra, P. S., Onasch, T. B., Brune, W. H., Hunter, J. F., Kroll, J. H.,
1044   Cummings, M. J., Brogan, J. F., Parmar, Y., Worsnop, D. R., Kolb, C. E., and Davidovits, P.:
1045   Effect of oxidant concentration, exposure time, and seed particles on secondary organic
1046   aerosol chemical composition and yield, Atmos. Chem. Phys., 15, 3063–3075,
1047   https://doi.org/10.5194/acp-15-3063-2015, 2015.
1048   Lehtipalo, K., Yan, C., Dada, L., Bianchi, F., Xiao, M., Wagner, R., Stolzenburg, D., Ahonen,
1049   L. R., Amorim, A., Baccarini, A., Bauer, P. S., Baumgartner, B., Bergen, A., Bernhammer, A.
1050   K., Breitenlechner, M., Brilke, S., Buchholz, A., Mazon, S. B., Chen, D., Chen, X., Dias, A.,
1051   Dommen, J., Draper, D. C., Duplissy, J., Ehn, M., Finkenzeller, H., Fischer, L., Frege, C.,
1052   Fuchs, C., Garmash, O., Gordon, H., Hakala, J., He, X., Heikkinen, L., Heinritzi, M., Helm, J.
1053   C., Hofbauer, V., Hoyle, C. R., Jokinen, T., Kangasluoma, J., Kerminen, V. M., Kim, C.,
1054   Kirkby, J., Kontkanen, J., Kürten, A., Lawler, M. J., Mai, H., Mathot, S., Mauldin, R. L.,
1055   Molteni, U., Nichman, L., Nie, W., Nieminen, T., Ojdanic, A., Onnela, A., Passananti, M.,

Petäjä, T., Piel, F., Pospisilova, V., Quéléver, L. L. J., Rissanen, M. P., Rose, C., Sarnela, N., Schallhart, S., Schuchmann, S., Sengupta, K., Simon, M., Sipilä, M., Tauber, C., Tomé, A., Tröstl, J., Väisänen, O., Vogel, A. L., Volkamer, R., Wagner, A. C., Wang, M., Weitz, L., Wimmer, D., Ye, P., Ylisirniö, A., Zha, Q., Carslaw, K. S., Curtius, J., Donahue, N. M., Flagan, R. C., Hansel, A., Riipinen, I., Virtanen, A., Winkler, P. M., Baltensperger, U., Kulmala, M., and Worsnop, D. R.: Multicomponent new particle formation from sulfuric acid, ammonia, and biogenic vapors, Sci. Adv., 4, 1–10, https://doi.org/10.1126/sciadv.aau5363, 2018.

Li, R., Palm, B. B., Ortega, A. M., Hlywiak, J., Hu, W., Peng, Z., Day, D. A., Knote, C., Brune, W. H., De Gouw, J. A., and Jimenez, J. L.: Modeling the radical chemistry in an oxidation flow reactor: Radical formation and recycling, sensitivities, and the OH exposure estimation equation, J. Phys. Chem. A, 119, 4418–4432, https://doi.org/10.1021/jp509534k, 2015.

Lu, K. D., Rohrer, F., Holland, F., Fuchs, H., Bohn, B., Brauers, T., Chang, C. C., Häseler, R., Hu, M., Kita, K., Kondo, Y., Li, X., Lou, S. R., Nehr, S., Shao, M., Zeng, L. M., Wahner, A., Zhang, Y. H., and Hofzumahaus, A.: Observation and modelling of OH and HO2 concentrations in the Pearl River Delta 2006: A missing OH source in a VOC rich atmosphere, Atmos. Chem. Phys., 12, 1541–1569, https://doi.org/10.5194/acp-12-1541-2012, 2012.

Ma, X., Tan, Z., Lu, K., Yang, X., Chen, X., Wang, H., Chen, S., Fang, X., Li, S., Li, X., Liu, J., Liu, Y., Lou, S., Qiu, W., Wang, H., Zeng, L., and Zhang, Y.: OH and HO2 radical chemistry at a suburban site during the EXPLORE-YRD campaign in 2018, Atmos. Chem. Phys., 22, 7005–7028, https://doi.org/10.5194/acp-22-7005-2022, 2022.

McMurry, P. H. and Grosjean, D.: Gas and Aerosol Wall Losses in Teflon Film Smog Chambers, Environ. Sci. Technol., 19, 1176–1182, https://doi.org/10.1021/es00142a006, 1985.

Mehra, A., Wang, Y., E. Krechmer, J., Lambe, A., Majluf, F., A. Morris, M., Priestley, M., J. Bannan, T., J. Bryant, D., L. Pereira, K., F. Hamilton, J., R. Rickard, A., J. Newland, M., Stark, H., Croteau, P., T. Jayne, J., R. Worsnop, D., R. Canagaratna, M., Wang, L., and Coe, H.: Evaluation of the chemical composition of gas- And particle-phase products of aromatic oxidation, Atmos. Chem. Phys., 20, 9783–9803, https://doi.org/10.5194/acp-20-9783-2020, 2020.

Mentel, T. F., Springer, M., Ehn, M., Kleist, E., Pullinen, I., Kurtén, T., Rissanen, M., Wahner, A., and Wildt, J.: Formation of highly oxidized multifunctional compounds: Autoxidation of peroxy radicals formed in the ozonolysis of alkenes - Deduced from structure-product relationships, Atmos. Chem. Phys., 15, 6745–6765, https://doi.org/10.5194/acp-15-6745-2015, 2015.

Mohr, C., Thornton, J. A., Heitto, A., Lopez-hil, F. D., Lutz, A., Riipinen, I., Hong, J., Donahue, N. M., Hallquist, M., Petäjä, T., Kulmala, M., and Yli-juuti, T.: Molecular identification of organic vapors driving atmospheric nanoparticle growth, Nat. Commun., 1–7, https://doi.org/10.1038/s41467-019-12473-2, 2019.

Molteni, U., Bianchi, F., Klein, F., Haddad, I. El, Frege, C., Rossi, M. J., Dommen, J., and Baltensperger, U.: Formation of highly oxygenated organic molecules from aromatic

compounds, Atmos. Chem. Phys, 18, 1909–1921, https://doi.org/10.5194/acp-18-1909-2018, 2018.

Müller, J. F., Liu, Z., Nguyen, V. S., Stavrakou, T., Harvey, J. N., and Peeters, J.: The reaction of methyl peroxy and hydroxyl radicals as a major source of atmospheric methanol, Nat. Commun., 7, 1–11, https://doi.org/10.1038/ncomms13213, 2016.

Ng, N. L., Canagaratna, M. R., Zhang, Q., Jimenez, J. L., Tian, J., Ulbrich, I. M., Kroll, J. H., Docherty, K. S., Chhabra, P. S., Bahreini, R., Murphy, S. M., Seinfeld, J. H., Hildebrandt, L., Donahue, N. M., Decarlo, P. F., Lanz, V. A., Prévôt, A. S. H., Dinar, E., Rudich, Y., and Worsnop, D. R.: Organic aerosol components observed in Northern Hemispheric datasets from Aerosol Mass Spectrometry, Atmos. Chem. Phys., 10, 4625–4641, https://doi.org/10.5194/acp-10-4625-2010, 2010.

Orlando, J. J. and Tyndall, G. S.: Laboratory studies of organic peroxy radical chemistry: An overview with emphasis on recent issues of atmospheric significance, Chem. Soc. Rev., 41, 6294–6317, https://doi.org/10.1039/c2cs35166h, 2012.

Otkjær, R. V., Jakobsen, H. H., Tram, C. M., and Kjaergaard, H. G.: Calculated Hydrogen Shift Rate Constants in Substituted Alkyl Peroxy Radicals, J. Phys. Chem. A, 122, 8665–8673, https://doi.org/10.1021/acs.jpca.8b06223, 2018.

Palm, B. B., Campuzano-Jost, P., Ortega, A. M., Day, D. A., Kaser, L., Jud, W., Karl, T., Hansel, A., Hunter, J. F., Cross, E. S., Kroll, J. H., Peng, Z., Brune, W. H., and Jimenez, J. L.: In situ secondary organic aerosol formation from ambient pine forest air using an oxidation flow reactor, Atmos. Chem. Phys., 16, 2943–2970, https://doi.org/10.5194/acp-16-2943-2016, 2016.

Peng, Z. and Jimenez, J. L.: Radical chemistry in oxidation flow reactors for atmospheric chemistry research, Chem. Soc. Rev., 49, 2570–2616, https://doi.org/10.1039/c9cs00766k, 2020.

Peng, Z., Day, D. A., Ortega, A. M., Palm, B. B., Hu, W., Stark, H., Li, R., Tsigaridis, K., Brune, W. H., and Jimenez, J. L.: Non-OH chemistry in oxidation flow reactors for the study of atmospheric chemistry systematically examined by modeling, Atmos. Chem. Phys., 16, 4283–4305, https://doi.org/10.5194/acp-16-4283-2016, 2016.

Praske, E., Otkjær, R. V., Crounse, J. D., Hethcox, J. C., Stoltz, B. M., Kjaergaard, H. G., and Wennberg, P. O.: Atmospheric autoxidation is increasingly important in urban and suburban North America, Proc. Natl. Acad. Sci. U. S. A., 115, 64–69, https://doi.org/10.1073/pnas.1715540115, 2018.

Pye, H. O. T., D'Ambro, E. L., Lee, B. H., Schobesberger, S., Takeuchi, M., Zhao, Y., Lopez-Hilfiker, F., Liu, J., Shilling, J. E., Xing, J., Mathur, R., Middlebrook, A. M., Liao, J., Welti, A., Graus, M., Warneke, C., de Gouw, J. A., Holloway, J. S., Ryerson, T. B., Pollack, I. B., and Thornton, J. A.: Anthropogenic enhancements to production of highly oxygenated molecules from autoxidation, Proc. Natl. Acad. Sci. U. S. A., 116, 6641–6646, https://doi.org/10.1073/pnas.1810774116, 2019.

Qi, X., Ding, A., Roldin, P., Xu, Z., Zhou, P., Sarnela, N., Nie, W., Huang, X., Rusanen, A., Ehn, M., Rissanen, M. P., Petäjä, T., Kulmala, M., and Boy, M.: Modelling studies of HOMs and their contributions to new particle formation and growth: comparison of boreal forest in Finland and a polluted environment in China, Atmos. Chem. Phys, 18, 11779–11791, https://doi.org/10.5194/acp-18-11779-2018, 2018.

Qiao, X., Yan, C., Li, X., Guo, Y., Yin, R., Deng, C., Li, C., Nie, W., Wang, M., Cai, R., Huang, D., Wang, Z., Yao, L., Worsnop, D. R., Bianchi, F., Liu, Y., Donahue, N. M., Kulmala, M., and Jiang, J.: Contribution of Atmospheric Oxygenated Organic Compounds to Particle Growth in an Urban Environment, Environ. Sci. Technol., https://doi.org/10.1021/acs.est.1c02095, 2021.

Qu, H., Wang, Y., Zhang, R., Liu, X., Huey, L. G., Sjostedt, S., Zeng, L., Lu, K., Wu, Y., Shao, M., Hu, M., Tan, Z., Fuchs, H., Broch, S., Wahner, A., Zhu, T., and Zhang, Y.: Chemical Production of Oxygenated Volatile Organic Compounds Strongly Enhances Boundary-Layer Oxidation Chemistry and Ozone Production, Environ. Sci. Technol., 55, 13718–13727, https://doi.org/10.1021/acs.est.1c04489, 2021.

Saunders, S. M., Jenkin, M. E., Derwent, R. G., and Pilling, M. J.: Protocol for the development of the Master Chemical Mechanism, MCM v3 (Part A): Tropospheric degradation of non-aromatic volatile organic compounds, Atmos. Chem. Phys., 3, 161–180, https://doi.org/10.5194/acp-3-161-2003, 2003.

Stolzenburg, D., Fischer, L., Vogel, A. L., Heinritzi, M., Schervish, M., Simon, M., Wagner, A. C., Dada, L., Ahonen, L. R., Amorim, A., Baccarini, A., Bauer, P. S., Baumgartner, B., Bergen, A., Bianchi, F., Breitenlechner, M., Brilke, S., Mazon, S. B., Chen, D., Dias, A., Draper, D. C., Duplissy, J., Haddad, I. El, Finkenzeller, H., Frege, C., Fuchs, C., Garmash, O., Gordon, H., He, X., Helm, J., Hofbauer, V., Hoyle, C. R., Kim, C., Kirkby, J., Kontkanen, J., Kürten, A., Lampilahti, J., Lawler, M., Lehtipalo, K., Leiminger, M., Mai, H., Mathot, S., Mentler, B., Molteni, U., Nie, W., Nieminen, T., Nowak, J. B., Ojdanic, A., Onnela, A., Passananti, M., Petäjä, T., Quéléver, L. L. J., Rissanen, M. P., Sarnela, N., Schallhart, S., Tauber, C., Tomé, A., Wagner, R., Wang, M., Weitz, L., Wimmer, D., Xiao, M., Yan, C., Ye, P., Zha, Q., Baltensperger, U., Curtius, J., Dommen, J., Flagan, R. C., Kulmala, M., Smith, J. N., Worsnop, D. R., Hansel, A., Donahue, N. M., and Winkler, P. M.: Rapid growth of organic aerosol nanoparticles over a wide tropospheric temperature range, Proc. Natl. Acad. Sci. U. S. A., 115, 9122–9127, https://doi.org/10.1073/pnas.1807604115, 2018.

Tan, Z., Fuchs, H., Lu, K., Hofzumahaus, A., Bohn, B., Broch, S., Dong, H., Gomm, S., Häseler, R., He, L., Holland, F., Li, X., Liu, Y., Lu, S., Rohrer, F., Shao, M., Wang, B., Wang, M., Wu, Y., Zeng, L., Zhang, Y., Wahner, A., and Zhang, Y.: Radical chemistry at a rural site (Wangdu) in the North China Plain: Observation and model calculations of OH, HO2 and RO2 radicals, Atmos. Chem. Phys., 17, 663–690, https://doi.org/10.5194/acp-17-663-2017, 2017.

Tan, Z., Rohrer, F., Lu, K., Ma, X., Bohn, B., Broch, S., Dong, H., Fuchs, H., Gkatzelis, G. I., Hofzumahaus, A., Holland, F., Li, X., Liu, Y., Liu, Y., Novelli, A., Shao, M., Wang, H., Wu, Y., Zeng, L., Hu, M., Kiendler-Scharr, A., Wahner, A., and Zhang, Y.: Wintertime photochemistry in Beijing: Observations of ROx radical concentrations in the North China Plain during the BEST-ONE campaign, Atmos. Chem. Phys., https://doi.org/10.5194/acp-18-12391-2018, 2018.

Tan, Z., Lu, K., Jiang, M., Su, R., Wang, H., Lou, S., Fu, Q., Zhai, C., Tan, Q., Yue, D., Chen, D., Wang, Z., Xie, S., Zeng, L., and Zhang, Y.: Daytime atmospheric oxidation capacity in four Chinese megacities during the photochemically polluted season: A case study based on box model simulation, Atmos. Chem. Phys., 19, 3493–3513, https://doi.org/10.5194/acp-19-3493-2019, 2019.

1187 Tröstl, J., Chuang, W. K., Gordon, H., Heinritzi, M., Yan, C., Molteni, U., Ahlm, L., Frege,
1188 C., Bianchi, F., Wagner, R., Simon, M., Lehtipalo, K., Williamson, C., Craven, J. S.,
1189 Duplissy, J., Adamov, A., Almeida, J., Bernhammer, A. K., Breitenlechner, M., Brilke, S.,
1190 Dias, A., Ehrhart, S., Flagan, R. C., Franchin, A., Fuchs, C., Guida, R., Gysel, M., Hansel, A.,
1191 Hoyle, C. R., Jokinen, T., Junninen, H., Kangasluoma, J., Keskinen, H., Kim, J., Krapf, M.,
1192 Kürten, A., Laaksonen, A., Lawler, M., Leiminger, M., Mathot, S., Möhler, O., Nieminen, T.,
1193 Onnela, A., Petäjä, T., Piel, F. M., Miettinen, P., Rissanen, M. P., Rondo, L., Sarnela, N.,
1194 Schobesberger, S., Sengupta, K., Sipilä, M., Smith, J. N., Steiner, G., Tomè, A., Virtanen, A.,
1195 Wagner, A. C., Weingartner, E., Wimmer, D., Winkler, P. M., Ye, P., Carslaw, K. S., Curtius,
1196 J., Dommen, J., Kirkby, J., Kulmala, M., Riipinen, I., Worsnop, D. R., Donahue, N. M., and
1197 Baltensperger, U.: The role of low-volatility organic compounds in initial particle growth in
1198 the atmosphere, Nature, 533, 527–531, https://doi.org/10.1038/nature18271, 2016.
1199 Tsiligiannis, E., Hammes, J., Salvador, C. M., Mentel, T. F., and Hallquist, M.: Effect of NOx
1200 on 1,3,5-trimethylbenzene (TMB) oxidation product distribution and particle formation,
1201 Atmos. Chem. Phys., 19, 15073–15086, https://doi.org/10.5194/acp-19-15073-2019, 2019.
1202 Vereecken, L.: Reaction Mechanisms for the Atmospheric Oxidation of Monocyclic Aromatic
1203 Compounds, Adv. Atmos. Chem., 377–527, https://doi.org/10.1142/9789813271838_0006,
1204 2019.
1205 Wang, L., Wu, R., and Xu, C.: Atmospheric oxidation mechanism of benzene. Fates of alkoxy
1206 radical intermediates and revised mechanism, J. Phys. Chem. A, 117, 14163–14168,
1207 https://doi.org/10.1021/jp4101762, 2013.
1208 Wang, M., Chen, D., Xiao, M., Ye, Q., Stolzenburg, D., Hofbauer, V., Ye, P., Vogel, A. L.,
1209 Mauldin, R. L., Amorim, A., Baccarini, A., Baumgartner, B., Brilke, S., Dada, L., Dias, A.,
1210 Duplissy, J., Finkenzeller, H., Garmash, O., He, X. C., Hoyle, C. R., Kim, C., Kvashnin, A.,
1211 Lehtipalo, K., Fischer, L., Molteni, U., Petäjä, T., Pospisilova, V., Quéléver, L. L. J.,
1212 Rissanen, M., Simon, M., Tauber, C., Tomé, A., Wagner, A. C., Weitz, L., Volkamer, R.,
1213 Winkler, P. M., Kirkby, J., Worsnop, D. R., Kulmala, M., Baltensperger, U., Dommen, J., El-
1214 Haddad, I., and Donahue, N. M.: Photo-oxidation of Aromatic Hydrocarbons Produces Low-
1215 Volatility Organic Compounds, Environ. Sci. Technol., 54, 7911–7921,
1216 https://doi.org/10.1021/acs.est.0c02100, 2020a.
1217 Wang, S., Wu, R., Berndt, T., Ehn, M., and Wang, L.: Formation of Highly Oxidized Radicals
1218 and Multifunctional Products from the Atmospheric Oxidation of Alkylbenzenes, Environ.
1219 Sci. Technol., 51, 8442–8449, https://doi.org/10.1021/acs.est.7b02374, 2017.
1220 Wang, W., Yuan, B., Peng, Y., Su, H., Cheng, Y., and Yang, S.: Direct observations indicate
1221 photodegradable oxygenated VOCs as larger contributors to radicals and ozone production in
1222 the atmosphere, Atmos. Chem. Phys., 1–28, 2022.
1223 Wang, Y., Mehra, A., Krechmer, J. E., Yang, G., Hu, X., Lu, Y., Lambe, A., Canagaratna, M.,
1224 Chen, J., Worsnop, D., Coe, H., and Wang, L.: Oxygenated products formed from OH-
1225 initiated reactions of trimethylbenzene: autoxidation and accretion, Atmos. Chem. Phys., 20,
1226 9563–9579, https://doi.org/10.5194/acp-20-9563-2020, 2020b.
1227 Whalley, L. K., Slater, E. J., Woodward-Massey, R., Ye, C., Lee, J. D., Squires, F., Hopkins,
1228 J. R., Dunmore, R. E., Shaw, M., Hamilton, J. F., Lewis, A. C., Mehra, A., Worrall, S. D.,
1229 Bacak, A., Bannan, T. J., Coe, H., Percival, C. J., Ouyang, B., Jones, R. L., Crilley, L. R.,
1230 Kramer, L. J., Bloss, W. J., Vu, T., Kotthaus, S., Grimmond, S., Sun, Y., Xu, W., Yue, S.,

1231 Ren, L., Joe, W., Nicholas Hewitt, C., Wang, X., Fu, P., and Heard, D. E.: Evaluating the

1232 sensitivity of radical chemistry and ozone formation to ambient VOCs and NOxin Beijing,

1233 Atmos. Chem. Phys., 21, 2125–2147, https://doi.org/10.5194/acp-21-2125-2021, 2021.

1234 Xu, L., Møller, K. H., Crounse, J. D., Kjaergaard, H. G., and Wennberg, P. O.: New insights

1235 into the radical chemistry and product distribution in the OH-initiated oxidation of benzene,

1236 Environ. Sci. Technol., 54, 13467–13477, https://doi.org/10.1021/acs.est.0c04780, 2020.

1237 Yan, C., Kocevska, S., and Krasnoperov, L. N.: Kinetics of the Reaction of CH3O2 Radicals

1238 with OH Studied over the 292-526 K Temperature Range, J. Phys. Chem. A, 120, 6111–6121,

1239 https://doi.org/10.1021/acs.jpca.6b04213, 2016.

1240 Yang, C., Yao, N., Xu, L., Chen, G., Wang, Y., Fan, X., Zhou, P., Clusius, P., Tham, Y. J.,

1241 Lin, Z., Chen, Y., Li, M., Hong, Y., and Chen, J.: Molecular Composition of Anthropogenic

1242 Oxygenated Organic Molecules and Their Contribution to Organic Aerosol in a Coastal City,

1243 Environ. Sci. Technol., 57, 15956–15967, https://doi.org/10.1021/acs.est.3c03244, 2023.

1244 Yao, L., Garmash, O., Bianchi, F., Zheng, J., Yan, C., Kontkanen, J., Junninen, H., Mazon, S.

1245 B., Ehn, M., Paasonen, P., Sipilä, M., Wang, M., Wang, X., Xiao, S., Chen, H., Lu, Y.,

1246 Zhang, B., Wang, D., Fu, Q., Geng, F., Li, L., Wang, H., Qiao, L., Yang, X., Chen, J.,

1247 Kerminen, V.-M., Petäjä, T., Worsnop, D. R., Kulmala, M., and Wang, L.: Atmospheric new

1248 particle formation from sulfuric acid and amines in a Chinese megacity, Science (80-.)., 361,

1249 278–281, https://doi.org/10.1126/science.aao4839, 2018.

1250 Yuan, B., Chen, W., Shao, M., Wang, M., Lu, S., Wang, B., Liu, Y., Chang, C. C., and Wang,

1251 B.: Measurements of ambient hydrocarbons and carbonyls in the Pearl River Delta (PRD),

1252 China, Atmos. Res., 116, 93–104, https://doi.org/10.1016/j.atmosres.2012.03.006, 2012.

1253 Zaytsev, A., Koss, A. R., Breitenlechner, M., Krechmer, J. E., Nihill, K. J., Lim, C. Y., Rowe,

1254 J. C., Cox, J. L., Moss, J., Roscioli, J. R., Canagaratna, M. R., Worsnop, D. R., Kroll, J. H.,

1255 and Keutsch, F. N.: Mechanistic study of the formation of ring-retaining and ring-opening

1256 products from the oxidation of aromatic compounds under urban atmospheric conditions,

1257 Atmos. Chem. Phys., 19, 15117–15129, https://doi.org/10.5194/acp-19-15117-2019, 2019.

1258 Zhao, Y., Thornton, J. A., and Pye, H. O. T.: Quantitative constraints on autoxidation and

1259 dimer formation from direct probing of monoterpene-derived peroxy radical chemistry, Proc.

1260 Natl. Acad. Sci., 115, 12142–12147, https://doi.org/10.1073/pnas.1812147115, 2018.

1261